Decoupling Capacity Fade and Voltage Decay of Li-rich Mn-rich Cathodes by Tailoring Surface Reconstruction Pathways

Authors: Gukhyun Lim,[abc] Min Kyung Cho,[d] Jaewon Choi,[e] Ke-Jin Zhou,[e] Dongki Shin,[bc] Seungyun Jeon,[abf] Minhyung Kwon,[a] A-Re Jeon,[a] Jinkwan Choi,[a] Seok Su Sohn,[c] Minah Lee,[a] Jihyun Hong,*[a]

[a]Department of Battery Engineering, Graduate Institute of Ferrous & Eco Materials Technology, Pohang University of Science and Technology (POSTECH), Pohang, 37667, Republic of Korea

[b]Center for Hydrogen Energy Materials, Korea Institute of Science and Technology (KIST), Seoul, 02792, Republic of Korea

[c]Department of Materials Science and Engineering, Korea University, Seoul, 02841, Republic of Korea

[d]Advanced Analysis and Data Center, Korea Institute of Science and Technology (KIST), Seoul, 02792, Republic of Korea

[e]Diamond Light Source, Harwell Campus, Didcot, OX11 0DE, UK

[f]Department of Chemical and Biological Engineering, Korea University, Seoul, 02841, Republic of Korea

Corresponding author: Prof. Jihyun Hong (ORCID: 0000-0001-7210-2901)

E-mail: jhong@postech.ac.kr

Table of Contents

Experimental details

Synthesis of LMR-NMC and XRD analysis

$Li_{1.17}Ni_{0.21}Mn_{0.55}Co_{0.07}O_2$ (LMR-NMC) was synthesized by a ball-milling assisted solid-state synthesis. Metal acetates (all from Sigma-Aldrich, >99% were combined in a ball-milling zirconia vessel in a molar ratio of 0.21:0.55:0.07:1.21 for Ni, Mn, Co, and Li, respectively. To compensate for loss at high annealing temperatures, a 3% molar excess of lithium acetate was added. The powders were then dissolved and mixed in ethanol. A zirconia wet-ball milling lasted for 12 hours in a planetary micro mill (Fritsch PULVERISETTE 7), alternating 10min of milling with 5min of rest to prevent excessive overheating. After ball-milling, the ethanol was evaporated, and the composite powder was sieved. The composite powder was heated at 500℃ for 6 hours in air to ensure complete the decomposition of the organic components. The resulting precursor was finely ground and annealed at 950℃ for 8 hours under the atmosphere. The Crystal structure of the LMR-NMC powder was analyzed using X-ray powder diffraction (XRD) with Cu-Kα radiation (D8 ADVANCE, Bruker AXS GmbH). The diffraction patterns were analyzed using the Rietveld refinement method using FullProf software.

Electrode fabrication

The synthesized LMR-NMC powder was mixed with Super-P (Timcal) and PVDF (Wellcos) in an 80:10:10 (having active material loading of 3-3.5 mg cm^{-2}) or 90:5:5 wt% ratio (for high-loading of ~8mg cm^{-2}). N-Methyl-2-pyrrolidone (NMP, Sigma-Aldrich, 99.5%, anhydrous) was added to form a slurry, which was blade-coated onto aluminum foil. The bladed slurry was dried at 80 °C in an ambient atmosphere for 12 hours. Disks of the desired size were punched, dried under vacuum at 100 °C for 24 hours, and subsequently transferred to an argon-filled glovebox (KOREA KIYON, Korea; O_2 and H_2O < 0.1 ppm). In the case of manufacturing graphite electrodes, graphite powder was mixed with conductive agent (Super-P+SWCNT) and a binder (SBR+CMC) in a ratio of 94:1.4:4.6 wt% (active material:conductive agent:binder to form a slurry. Distilled water was added to form a slurry, which was blade-coated on a copper foil current collector. The films were dried at 80 °C in an ambient atmosphere for 12 hours. Disks of the desired size were punched, dried further at 80 °C under vacuum for 24 hours.

Electrochemical tests

A 2032-type coin cell was assembled with an 11.3 mm diameter LMR-NMC cathode and a 19 mm diameter Celgard 2325 separator, soaked in 100 µl of electrolyte. In LMR-NMC||Li half cells, a 16 mm diameter Li metal (with a thickness of 450 µm) was used as the anode. In LMR-NMC||graphite full cells, a 12 mm diameter graphite electrodes with an N/P ratio of 1.1 were used. Except for the cycling experiment at high active material loading (~8 mg cm^{-2}) in Figure S6, cathode electrodes with the loading of 3.0-3.5 mg cm^{-2} were used in all other experiments. Various types of electrolytes were used: 1 M $LiPF_6$ in DMC (1LPDMC), 1.5 M $LiPF_6$ in DMC (1.5LPDMC), 2.0 M $LiPF_6$ in DMC (2LPDMC), 1 M $LiPF_6$ in EC/DMC (1:1 vol) (1 M LP30), and 1.5 M $LiPF_6$ in EC/DMC (1:1 vol) (1.5 M LP30). To prepare the EC-free electrolytes (1-2LPDMC), DMC solvent (Sigma-Aldrich, 99% anhydrous) was dried with molecular sieves for 24h before use. The LMR-NMC||Li half cells were cycled on a battery tester (WonAtech,

WBCS3000) within a voltage range of 2.0-4.8 V (vs. Li), and the LMR-NMC||graphite full cells were run within a range of 1.85-4.75 V. All coin cells underwent three formation cycles at 0.06C (1C=250 mA g^{-1}). Although the theoretical capacity of LMR-NMC is 361 mAh g^{-1}, we set a practical capacity of 250 mAh g^{-1}, based on the formation cycle, as 1C. For testing graphite half cells, we cycled the cells with a voltage range of 5 mV-1 V (vs. Li) at 10mA g^{-1}. Galvanostatic intermittent titration technique (GITT) was performed with 1-hour constant current pulses at 0.06 C, followed by 3 hours of open circuit potential (OCP) after each pulse. Potential-controlled electrochemical impedance spectroscopy (EIS) was conducted in a frequency range of 100 kHz to 10 mHz with an AC voltage perturbation of 10 mV (BioLogic, VMP3).

Electrochemical protocol: 'progressive opening of potential windows'

The asymmetric anion reaction exhibits voltage hysteresis during the electrochemical cycling, a process we refer to as the 'progressive opening of potential windows.' This protocol involves gradually elevating charge cutoff voltage from 3.50 V to 3.70, 3.95, 4.10, 4.30, 4.50, and 4.80 V, with a fixed starting voltage of 2.0 V in each cycle. When the charge cutoff voltage increases beyond 4 V, where anion redox is predominantly expressed, the discharge voltage at the same SOC lowers due to the increase of the oxidized oxygen anions enabled in the low voltage regime during discharge.

Transmission electron microscopy (TEM)

For ex-situ analysis, all coin cells were disassembled in a glove box within an argon environment, washed with dimethyl carbonate (DMC), and dried in a vacuum state in the antechamber of the glove box for an hour. The active materials were scraped from the rinsed electrode and dispersed in DMC in an Ar-filled glove box. The dispersion solution was dropped onto Cu grids and dried. A transmission electron microscope (TEM) with the probe aberration corrector, Titan 80-300TM (Thermofisher, Netherlands), operated at 300 kV, was used to analyze the microstructure of the LMR-NMC particles after cycling. This microscope can provide a probe size of about 1 Å in diameter and 0.8 Å in spatial resolution.

Synchrotron-based X-ray absorption spectroscopies

Synchrotron radiation-based experiments were performed at Pohang light source-II (PLS-II), Pohang, South Korea. Soft X-ray absorption spectroscopy (sXAS) experiment was conducted at the 8A1 SPEM and 10D KIST NEXAFS beamlines. The prepared samples were attached to the sample holder in the glove box, and the holder was sealed in an aluminum pouch to prevent air exposure and moved to the vacuum chamber of the sXAS equipment. All sXAS spectra were collected, background subtracted, and normalized for the incident photon flux measured by inserting a gold (Au) mesh in the path of the X-ray beam.

For hard X-ray absorption fine structure spectroscopy (XAFS) measurements, in-situ XAFS was performed at the 8C Nano XAFS beamline, and ex-situ XAFS was conducted at the 10C Wide XAFS beamline. *Operando* Mn K-edge XANES measurement was conducted with Al pouch cells pressured by the Be windows at a current density of 0.06 C. For *ex-situ* analysis, all samples were prepared in an Ar-filled glove box and contained in sealed Al pouches to avoid air exposure. The XAFS data were processed using ATHENA software.

High-resolution resonant inelastic X-ray scattering (RIXS)

High-resolution resonant inelastic x-ray scattering (RIXS) experiments on cycled LMR-NMCs were conducted at the I21 RIXS beamline of Diamond Light Source, United Kingdom. The samples were prepared using a standard procedure that avoids any possible exposure to air; we glued them on the holder in a glove box and transferred them to the load-lock chamber using a vacuum suitcase. The pressure inside the main experimental chamber was maintained under ultra-high-vacuum conditions of ~10^{-10} mbar. The sample holder was mounted on a six-circle manipulator, thermally anchored to a ^{4}He flow cryostat which maintains the sample temperature at 70 K. We collected XAS spectra to tune the energy of the incident x-ray beam at the O K-edge resonant energy (~531 eV). Energy-dependent RIXS maps were obtained in a range between 527 and 535eV.

We optimized the scattering geometry and beamline parameters to maximize the throughput of outgoing X-ray beam while maintaining a sufficiently high resolution for resolving the vibration features of molecular O_2. The grazing-in geometry with an incident angle $\theta = 20^{\circ}$ was employed to improve the signal yield. The linear vertical (LV, or σ) polarization was used. The background intensity was reduced by fixing the scattering angle (2θ) to 90°. A paraboloidal collecting mirror vastly improves the throughput of the scattered X-ray beam. Finally, we achieved an energy resolution of 42 meV at O K-edge with an exit slit opening of 50 µm.

Liquid ^{1}H Nuclear magnetic resonance (NMR)

After cycling the LMR-NMC/Li cells, the cells were disassembled in an argon-filled glovebox and the Celgard 2325 separator was soaked in 1.0 mL of DMSO-d_6(Aldrich, 99.9%) for 5 minutes. The solution was transferred to an airtight NMR tube. One-dimensional 1H NMR spectra were recorded on a Bruker AVANCE III 500 (500 MHz) spectrometer. 1H spectra were internally referenced to DMSO-d_6 at 2.50 ppm.

ICP-AES for measuring the amount of transition metals dissolution

We used an inductively coupled plasma atomic emission spectrometry (ICP-AES) at Research institute of industrial science & technology (RIST) to measure the amount of transition metals (Mn, Ni, and Co) dissolved from the cycled LMR-NMC cathodes. After cycling the cells, we disassembled the cells and retrieved the cathodes and Li metals. All coin cell components, except for the cathode and Li metal, were dipped in distilled water, and the solution was collected to measure the concentration of dissolved transition metals from the electrolyte. Additionally, to analyze the transition metals that migrated to the Li metal anode, we dissolved the detached Li metal using distilled water and a pre-treatment acid solution. By combining the two pre-treatment solutions and adjusting the volume with distilled water under consistent conditions, we were able to compare the concentration of transition metals.

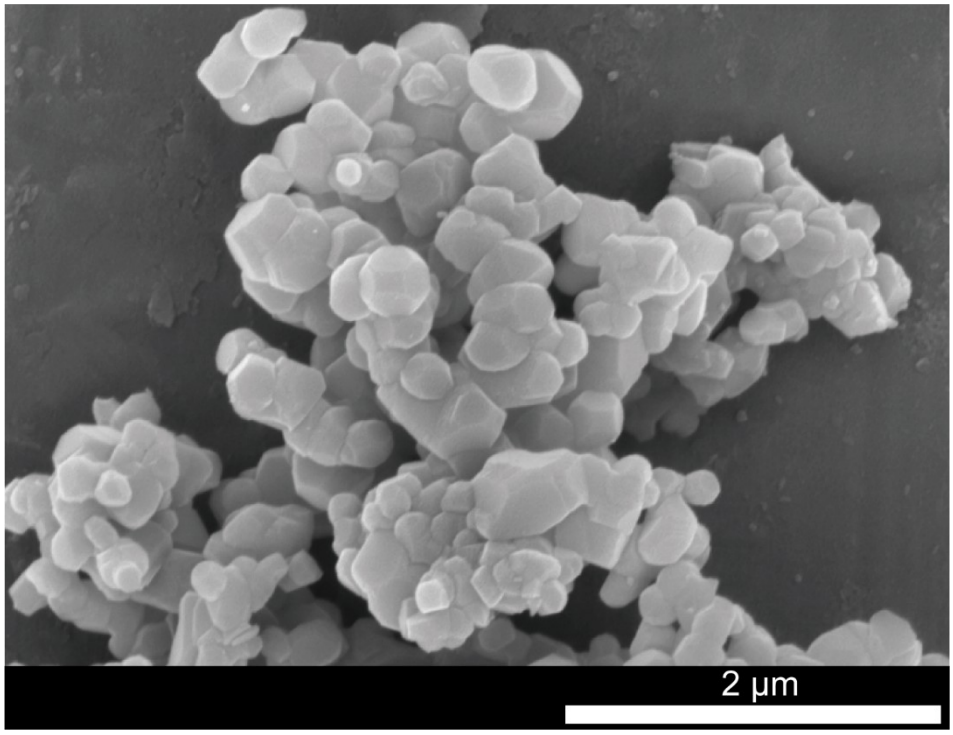

Fig. S1 SEM image of the synthesized LMR-NMC particles with a size distribution of 100-400 nm.

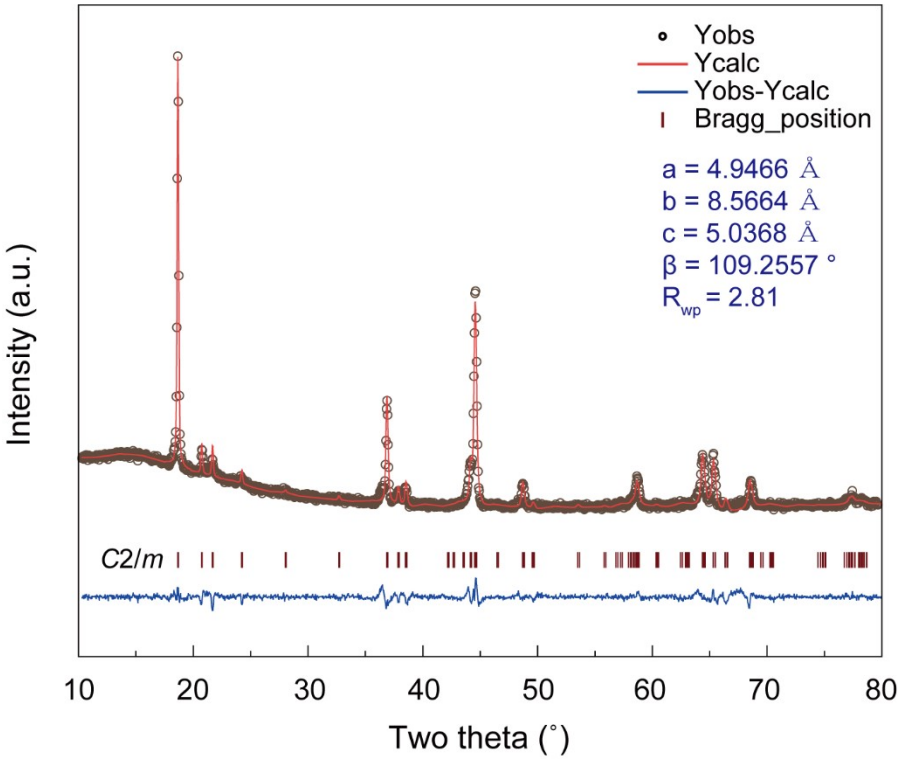

Fig. S2 The Rietveld refinement result for the synthesized LMR-NMC powder with the space group of *C*2/*m*. The lattice parameters obtained from the refinement are consistent with those reported in previous studies[1-4].

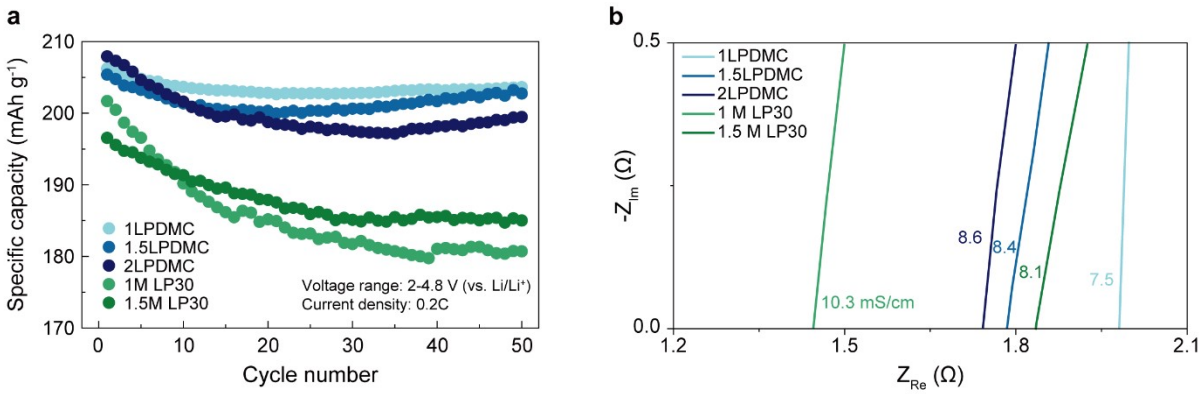

Fig. S3 (a) Cycling tests of LMR-NMC||Li cells (CAM: 3-3.5 mg cm^{-2}, t_{Li}: 450 µm) with 1 M $LiPF_6$ in DMC (1LPDMC), 1.5 M $LiPF_6$ in DMC (1.5LPDMC), 2.0 M $LiPF_6$ in DMC (2LPDMC), 1 M $LiPF_6$ in EC/DMC (1:1 vol) (1 M LP30), and 1.5 M $LiPF_6$ in EC/DMC (1:1 vol) (1.5 M LP30). (b) Ionic conductivity of electrolytes, obtained by EIS analysis of stainless-steel symmetric cells. We used the equation of σ (ionic conductivity) = L R^{-1} A^{-1} to calculate the ionic conductivity. 'L' is the distance between two stainless electrodes, determined by measuring the thickness of a separator retrieved from the disassembled cells. 'A' equals to the area of electrodes. 'R' is the resistance, measured by reading Z_{Re} when $-Z_{Im}$ is zero.

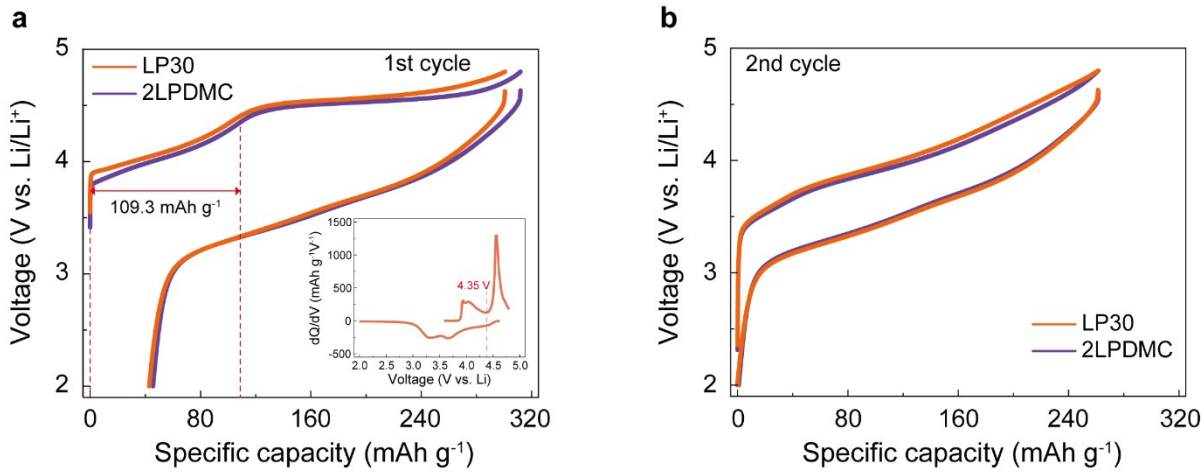

Fig. S4 The voltage profiles of LMR-NMC||Li cells (CAM: 3-3.5 mg cm^{-2}, t_{Li}: 450 µm) were investigated during the **(a)** first and **(b)** second formation cycles, employing both LP30 and 2LPDMC electrolytes at a constant current density of 0.06C. The overall profiles remained similar, exhibiting approximately 109 mA g^{-1} for cation (Ni+Co) redox, which occurs up to 4.35 V during charging (see dQ/dV profile in Fig. S3 (a)).

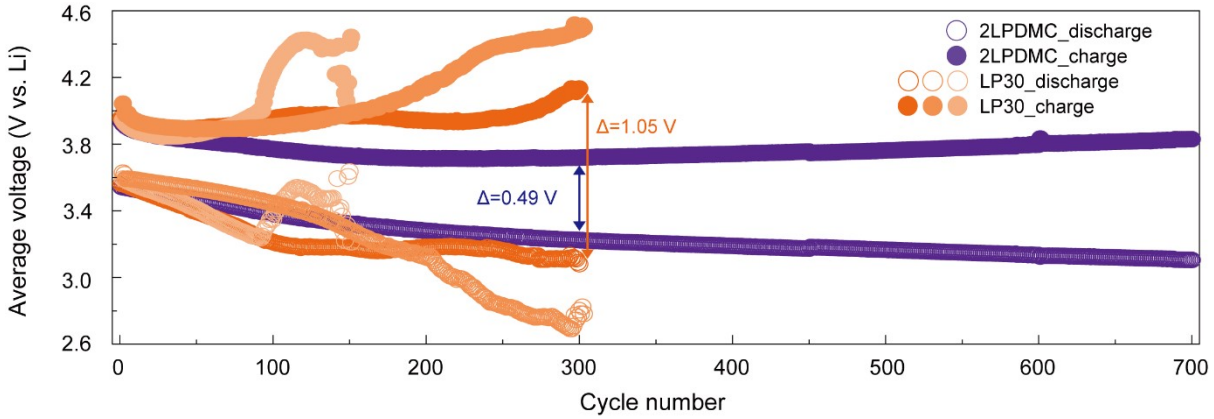

Fig. S5 The Average charge and discharge voltage of LMR-NMC||Li cells (CAM: 3-3.5 mg cm^{-2}, t_{Li}: 450 μm) at 0.2C during long-term cycling with the LP30 and 2LPDMC electrolytes. After 300 cycles, the gaps between average charge and discharge voltage were 1.05 V for LP30 and 0.49 V for the 2LPDMC, respectively. This result indicates that the capacity loss and potential fade of LMR-NMC, which are simultaneously observed under conventional cycling conditions using EC-containing electrolytes, can be attributed to sluggish kinetics. This kinetic polarization factor has limited the complete understanding of the thermodynamic changes in LMR-NMC.

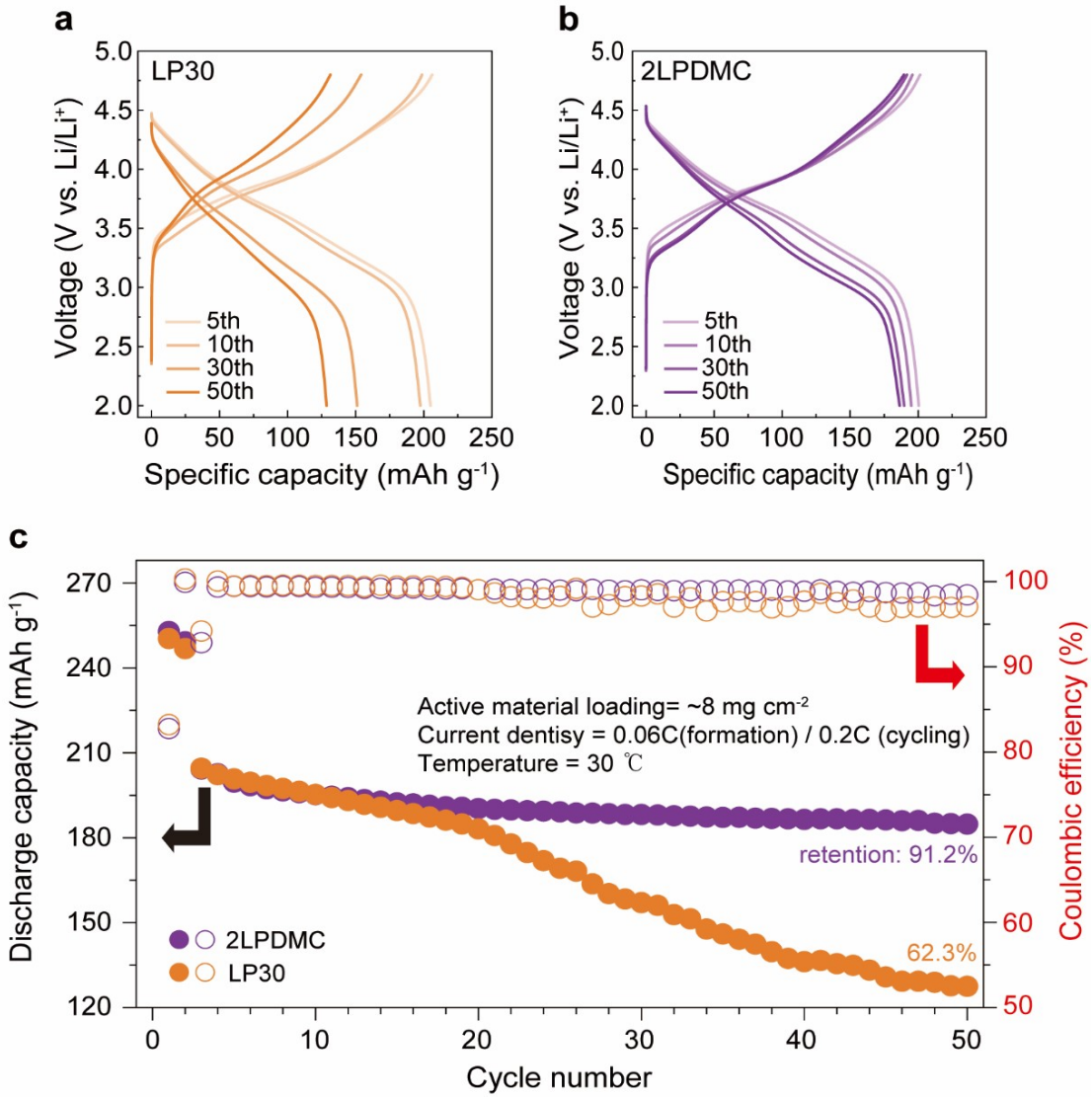

Fig. S6 Cycling performance of LMR-NMC||Li cells (CAM: 3-3.5 mg cm^{-2}, t_{Li}: 450 µm) with a high active material loading of 8 mg cm^{-2} at 0.2 C in the LP30 and 2LPDMC electrolytes: Voltage profiles for the 5th, 10th, 30th, and 50th cycles using **(a)** LP30 and **(b)** 2LPDMC, and **(c)** capacity and CE plot. When using LP30, accelerated degradation due to the high active material loading leads to a significant overpotential increase and capacity loss. In contrast, when using the 2LPDMC electrolyte, the overpotential is suppressed, resulting in superior cycle life compared to previous studies[5-7].

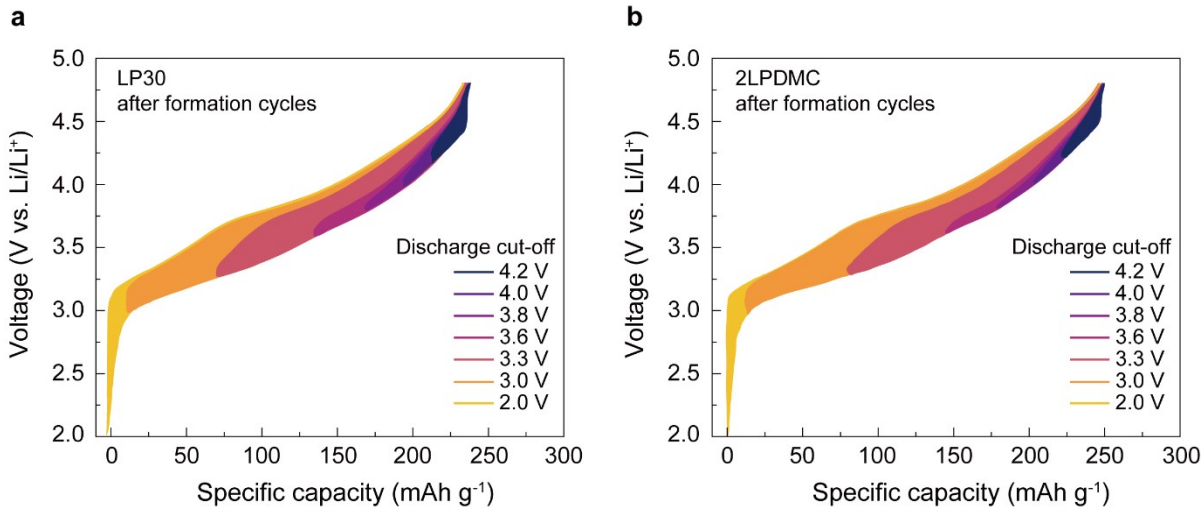

Fig. S7 Voltage profiles of LMR-NMC||Li cells (CAM: 3-3.5 mg cm^{-2}, t_{Li}: 450 µm) cycled with progressive opening of discharge potential windows were observed after formation cycles in **(a)** LP30 and **(b)** 2LPDMC, respectively. Prior to discharging to various discharge cutoff voltages; 4.2, 4.0, 3.8, 3.6, 3.3, 3.0, and 2.0 V (vs. Li), the cells were charged to 4.8 V in every cycle. The current density was 0.06 C. The voltage profiles and hysteresis exhibited similar trends in both electrolytes. When the discharge cutoff voltage is lowered, the charge voltage at the same state of charge (SOC) increases, owing to the reduction of oxidized oxygen anions in the low voltage regime.

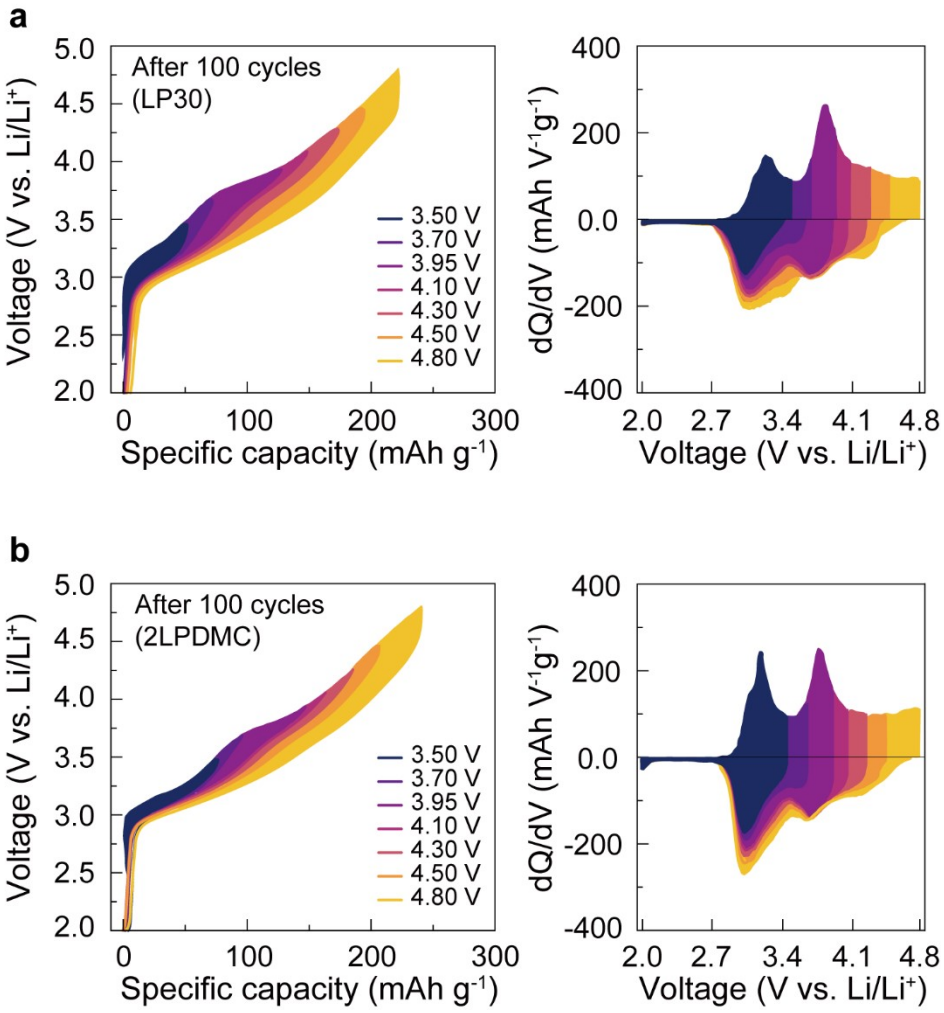

Fig. S8 Voltage profiles and corresponding dQ/dV curves of LMR-NMC||Li cells (CAM: 3-3.5 mg cm^{-2}, t_{Li}: 450 µm) during the progressive opening of charge potential windows were observed after 100 cycles with the **(a)** 2LPDMC and **(b)** LP30 electrolytes, respectively. Before charging to various charge cutoff voltages; 3.5, 3.7, 3.95, 4.1, 4.3, 4.5, and 4.8 V (vs. Li), the cells were discharged to 2.0 V in each cycle. The current density was 0.06 C. The 2LPDMC caused a significantly higher capacity near 3.0 V and 4.7 V for both charge and discharge, with less voltage hysteresis compared to the LP30. This lower hysteresis indicates a greater contribution from symmetric cation redox.

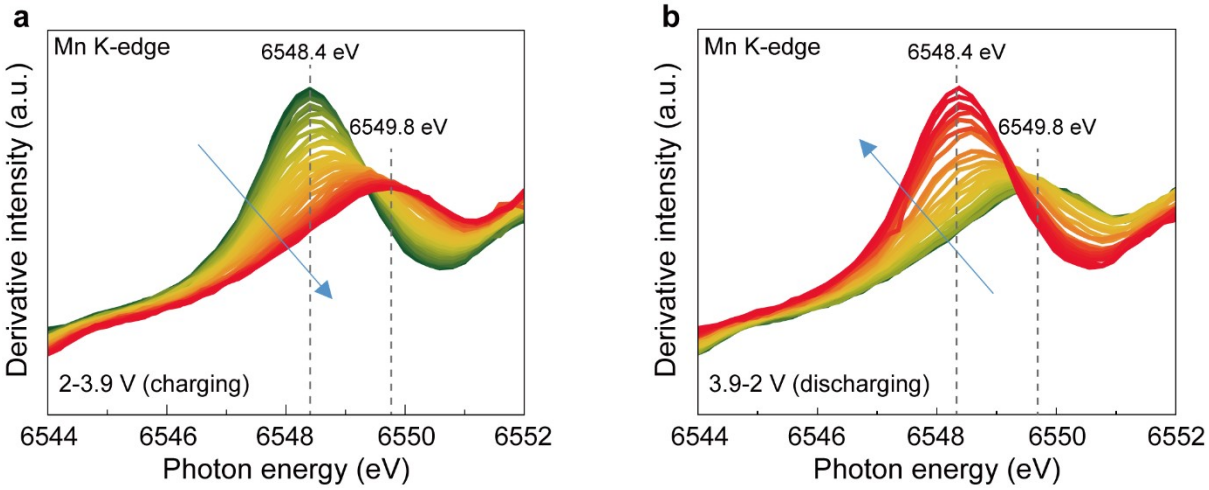

Fig. S9 Derivatives of *operando* Mn K-edge XANES spectra of the cycled LMR-NMC during **(a)** charging and **(b)** discharging with the 2LPDMC reveal a reversible energy shift of approximately 1.36 eV within the voltage range of 2 to 3.9 V (vs. Li). Given the linear correlation between the Mn oxidation state and the inflection point energy[8], the calculated change in Mn valence of 0.68 suggests significant formation of the Mn-active phase, such as a spinel phase, throughout the active material.

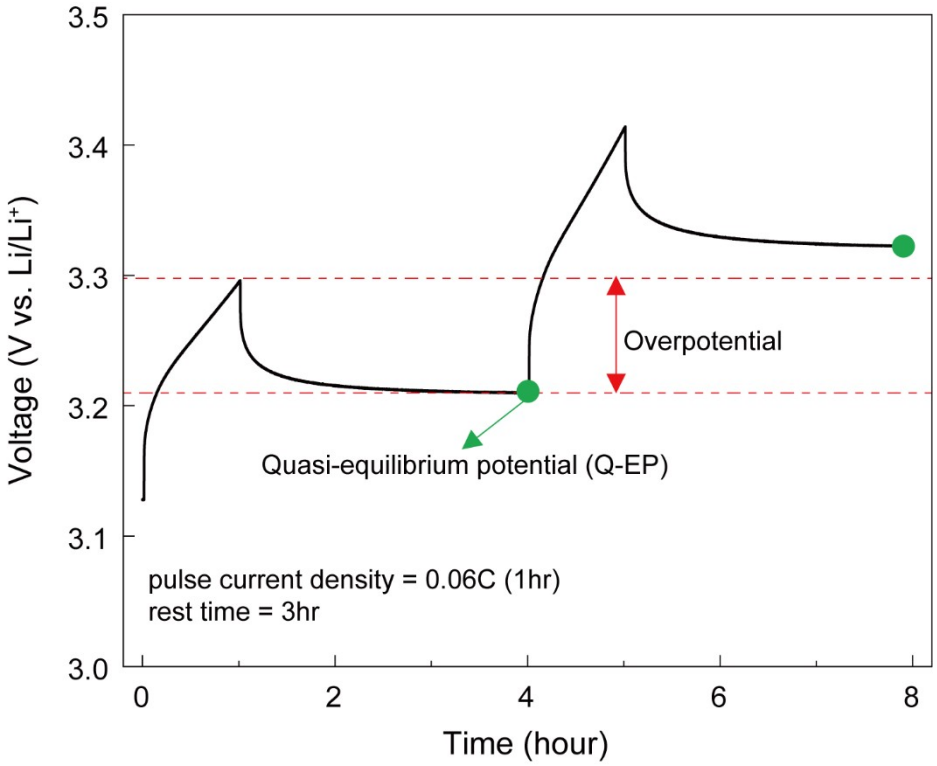

Fig. S10 The schematic illustrates the Galvanostatic Intermittent Titration Technique (GITT), where potential changes over time during a current pulse and subsequent relaxation period. A current pulse, with a current density of 0.06C, was applied for 1hour, followed by a relaxation period of 3 hours. The Quasi-Equilibrium Potential (Q-EP) represents the equilibrium potential after relaxation, and the overpotential is calculated as the difference in potential between the start and end-points of the relaxation period.

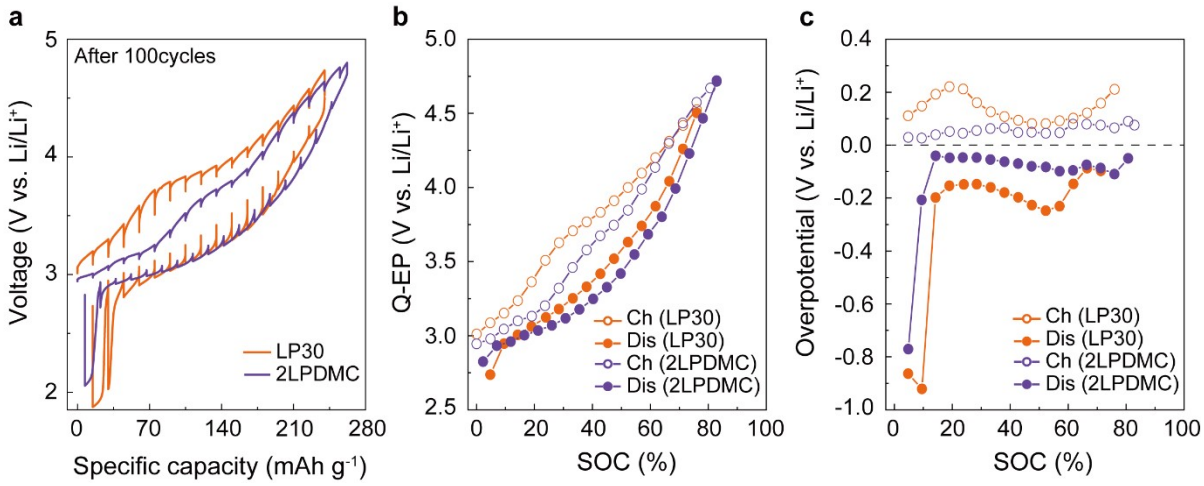

Fig. S11 (a) GITT profiles of the LMR-NMC||Li cells (CAM: 3-3.5 mg cm^{-2}, t_{Li}: 450 µm) with both LP30 and 2LPDMC after 100 cycles. **(b)** Quasi-equilibrium potential (Q-EP) and **(c)** overpotential, corresponding to state of charge (SOC), were derived from the GITT profiles. The decrease in Q-EP at the same SOC is more pronounced for the cathode cycled in the 2LPDMC, indicating more rigorous thermodynamic and structural changes. In addition, the overpotential of LMR-NMC with the LP30 is higher than that with the 2LPDMC in all SOCs.

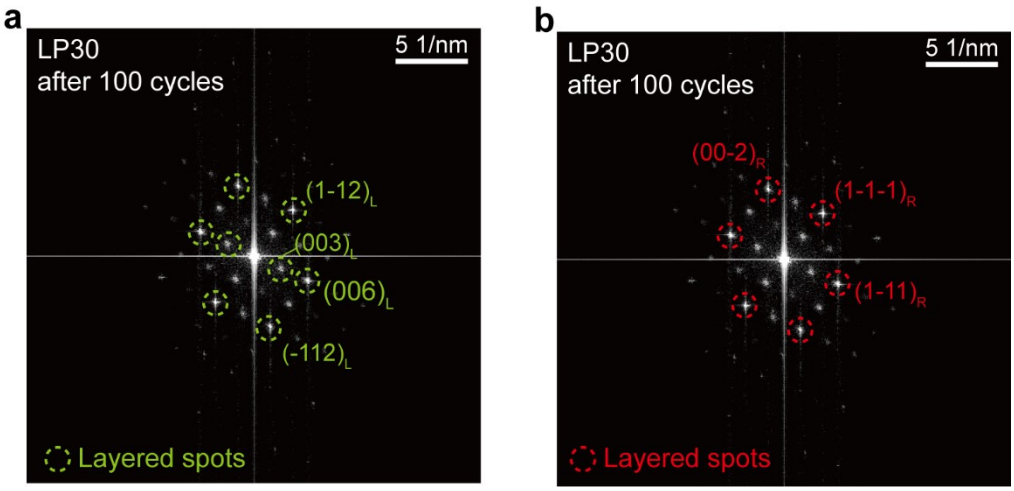

Fig. S12 The FFT patterns of the cycled LMR-NMC, marked with (a) layered phase (green) and (b) rocksalt phase (red). The spots that do not correspond to either the layered or rocksalt phases are diffraction spots of the spinel phase. All the rocksalt spots overlapped with those of the layered phase. On the other hand, in the case of the spinel phase, there are unique diffraction spots [(1-11), (002), (2-20), and (1-13)] that belong exclusively to the spinel phase.

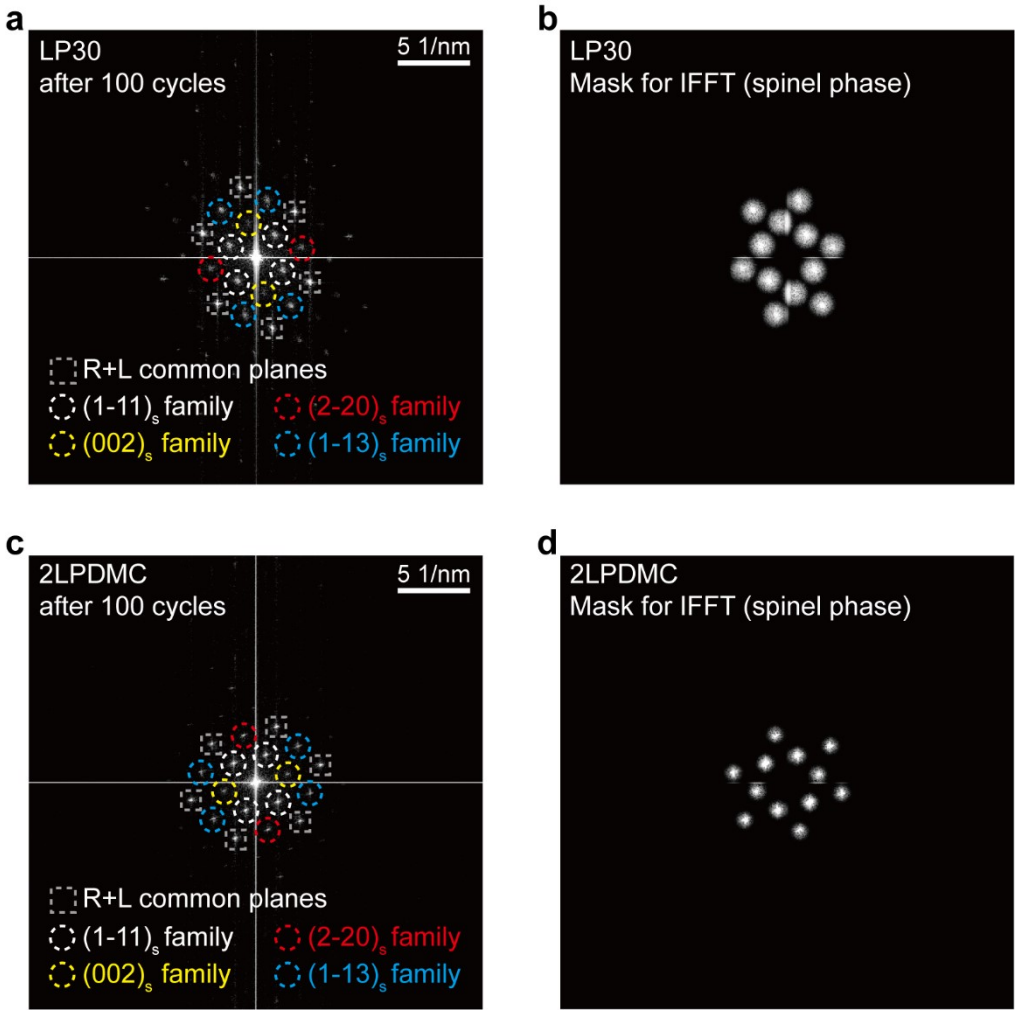

Fig. S13 The FFT patterns and masks for IFFT of the LMR-NMC cycled with the **(a), (b)** LP30 and **(c), (d)** 2LPDMC. In order to highlight the spinel phase area in each image (Figs. 3(a) and 3(d)) through IFFT, masks were applied to spots unique to the spinel phase. In this context, 'R', 'L', and 'S' denote rocksalt, layered, and spinel phases, respectively.

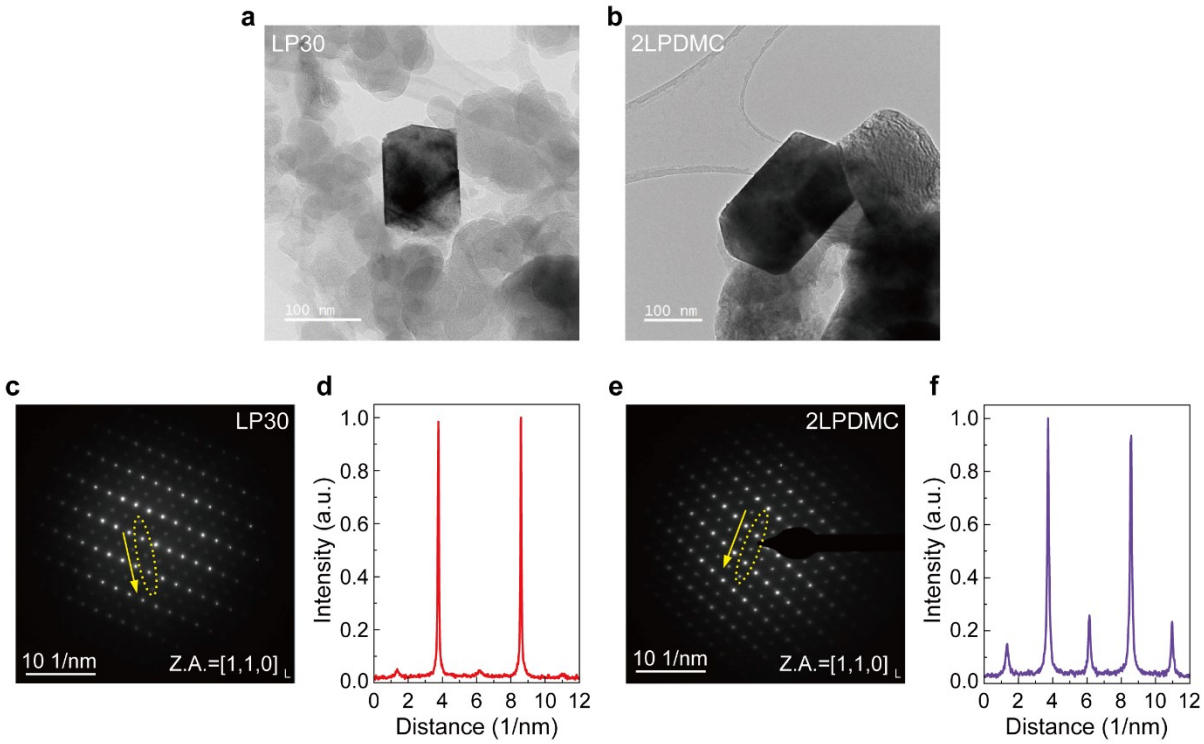

Fig. S14 TEM images display the entire particles corresponding to SAD patterns of the LMR-NMC cycled with **(a)** LP30 and **(b)** 2LPDMC electrolytes. Due to small diameter of less than 200 nm, the SAD patterns of these particles serve as indicators of the average crystallinity of the bulk. The SAD patterns and histogram of the points lying in the $[1\bar{1}3]$ direction of LMR-NMC with the **(c), (d)** LP30, and **(e), (f)** 2LPDMC.

The SAD pattern of the cycled LMR-NMC show bright diffraction spots of the layered phase and faint extra spots of the spinel phase, for both electrolytes. The diffraction from the spinel phase was more substantial for the 2LPDMC than LP30 by 180-360% in intensity, the result confirms the more rigorous layered-to-spinel phase transition at the bulk level in the 2LPDMC. On the other hand, unlike the FFT of the surface regions, the characteristics of the rocksalt phase in the SAD were negligible, indicating that the layered-to-rocksalt phase transition mainly occurred at the particle surface only after cycling in LP30.

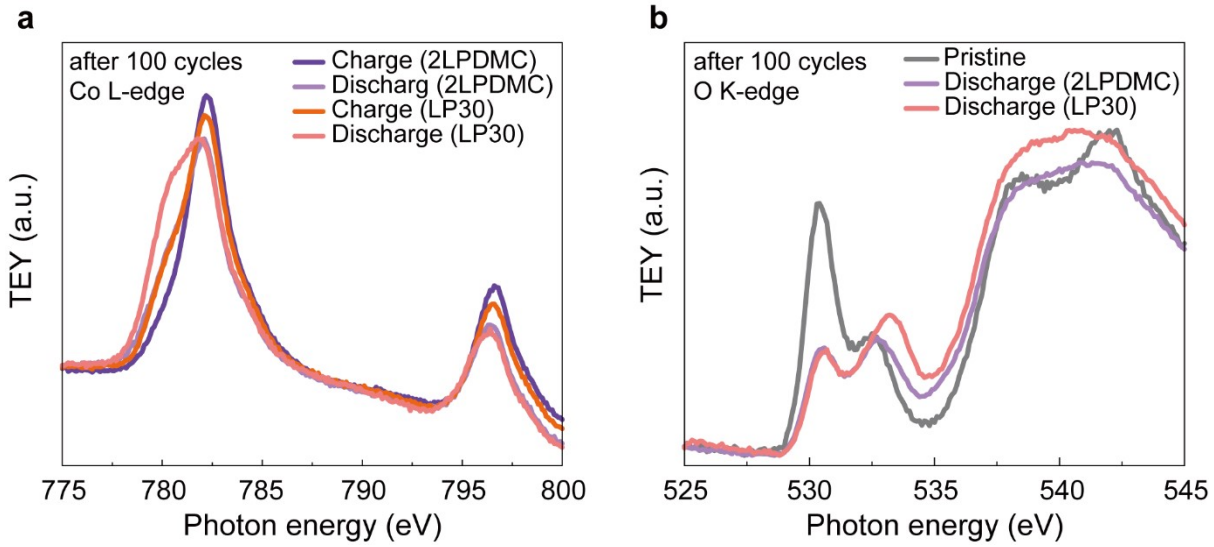

Fig. S15 (a) Co $L_{2,3}$-edge and **(b)** O K-edge sXAS-TEY spectra of the LMR-NMC electrodes after 100 cycles at 0.2C with both LP30 and 2LPDMC. It is noteworthy that a more reduced oxidation state of transition metals remains when using the LP30 electrolyte.

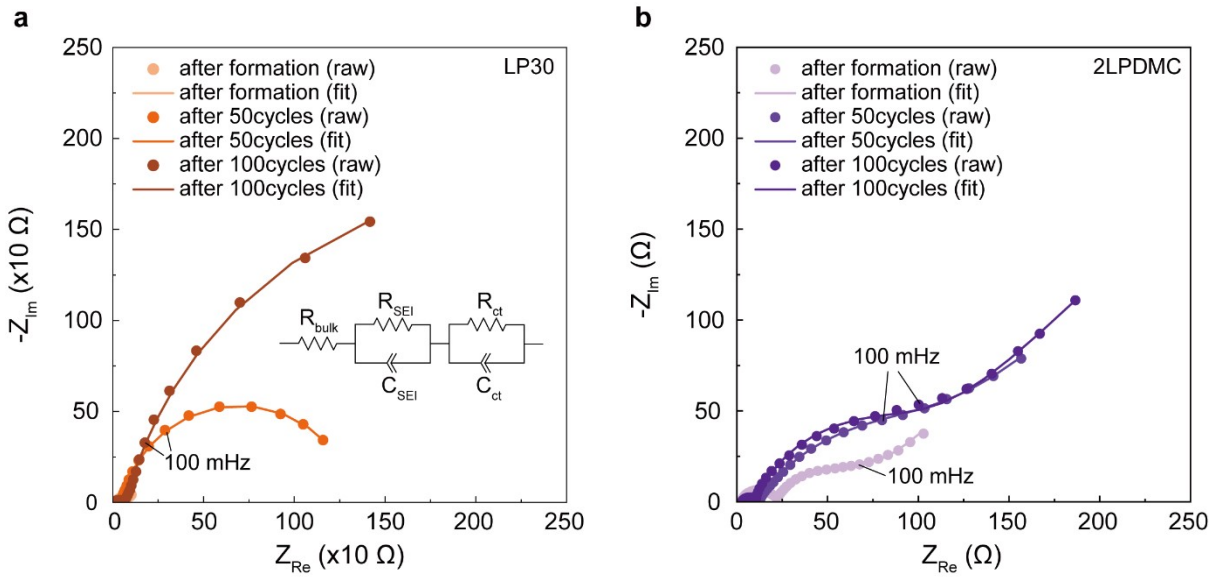

Fig. S16 EIS curves of the LMR-NMC||Li cells (CAM: 3-3.5 mg cm^{-2}, t_{Li}: 450 µm) after formation, and after 50 and 100 cycles with the **(a)** LP30 and **(b)** 2LPDMC. The measurements were conducted at 3.5 V (vs. Li). There was a much more pronounced increase in the resistance of the second semi-circle, indicative of charge transfer resistance (R_{ct}), with the LP30 electrolyte. The substantial R_{ct} increase in LP30 is due to the absence of Li-diffusion paths in the rocksalt crystal structure, which provokes the failure of the LMR-NMC.

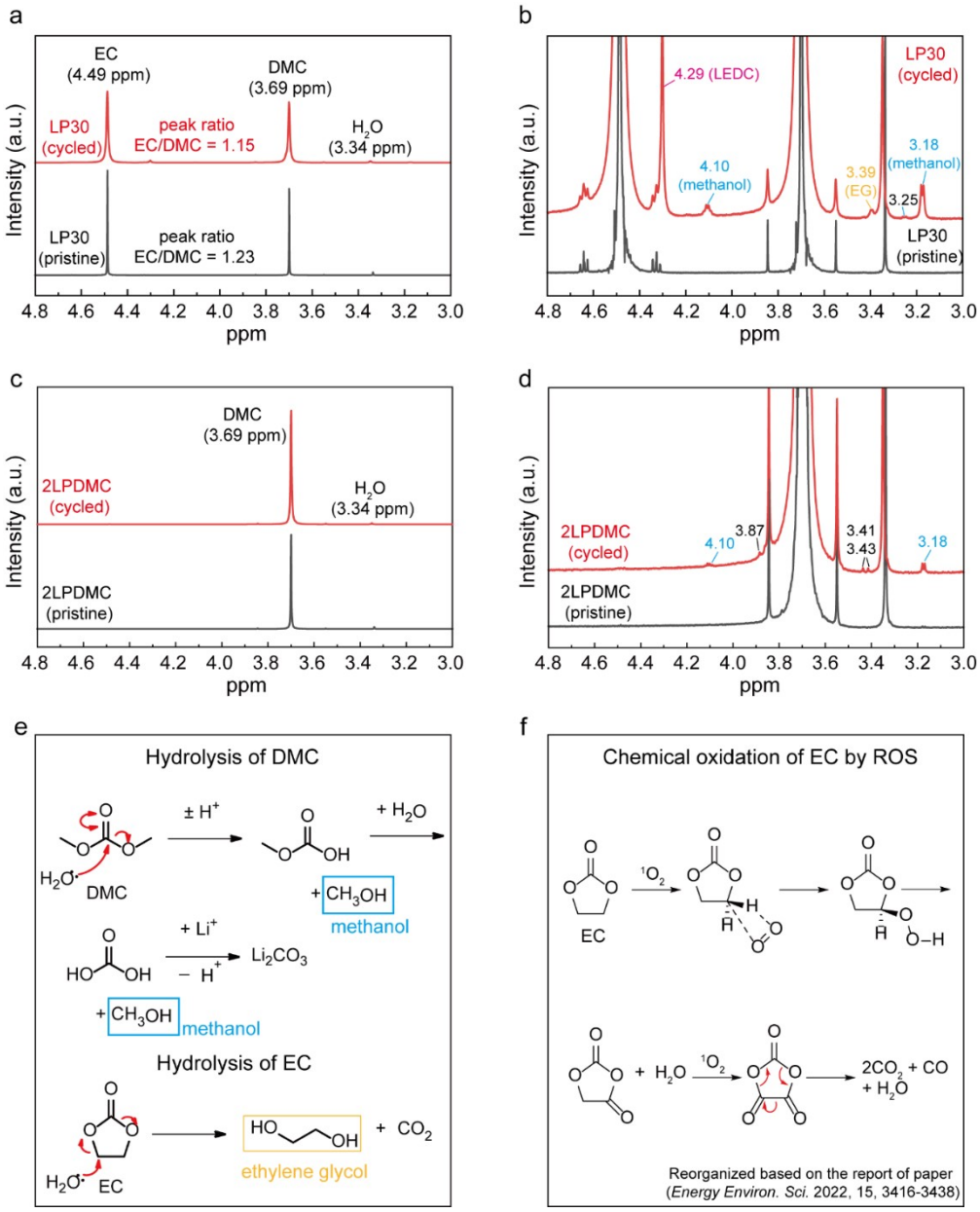

Fig. S17 The ^{1}H NMR spectra of solutions containing the **(a-b)** LP30 **and (c-d)** 2LPDMC electrolytes. The ^{1}H NMR spectrum of solutions containing LP30 showed significant formation of ethylene glycol (3.39 ppm, orange color) and methanol (3.18 and 4.10 ppm, blue color) byproducts after long-term cycling, which can be induced by **(e)** hydrolysis of EC and DMC, respectively[9-12]. The prominent formation of methanol and ethylene glycol can be attributed to the large amount of moisture generated as byproducts, indicating that the emission of singlet oxygen from the lattice of active material occurred during cycling, followed by **(f)** a side reaction with EC (EC + $^{1}O_2 \rightarrow 2CO_2 + CO + 2H_2O$)[9, 10, 12-17]. We also observed that EC was reduced upon contact with the Li metal anode, forming lithium ethylene dicarbonate (LEDC, 4.29 ppm, magenta color)[12].

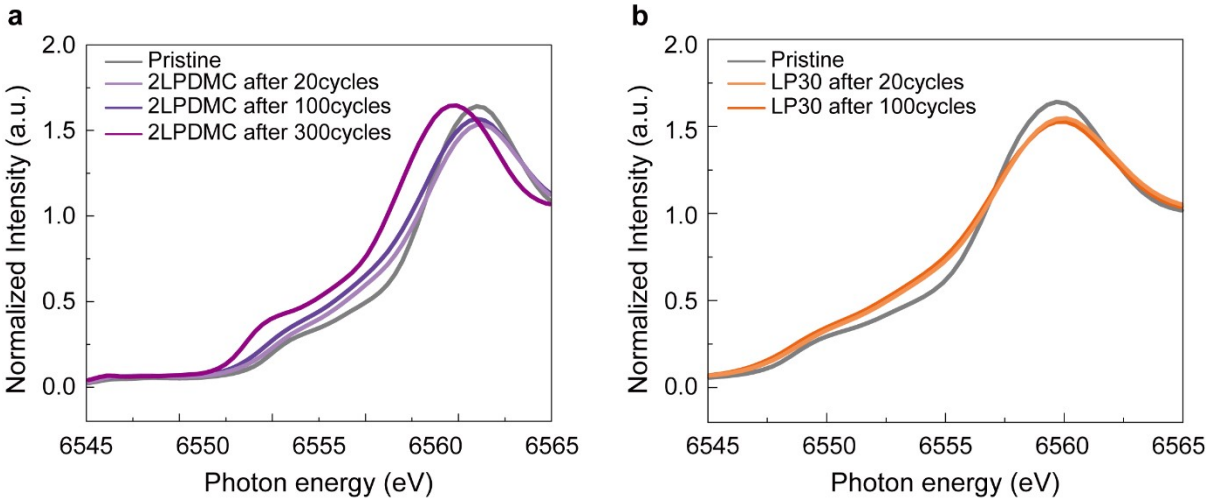

Fig. S18 Mn K-edge XANES spectra of the discharged LMR-NMC electrodes after cycling with **(a)** 2LPDMC and **(b)** LP30 electrolytes. After short-term cycling (20 cycles), LMR-NMCs exhibit a similar degree of Mn reduction in both electrolytes. During long-term cycling, while further Mn reduction is barely observed in LP30, more significant Mn reduction is noted in 2LPDMC. After 300 cycles, considerable Mn reduction extends into the bulk due to the layered-to-spinel phase transition.

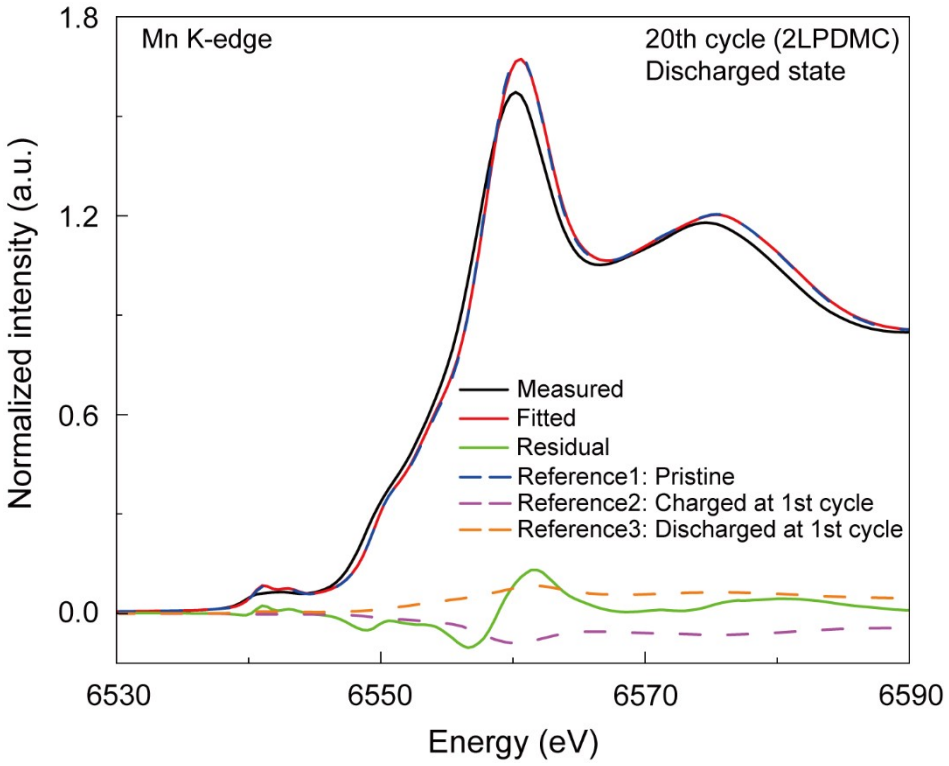

Fig. S19 A linear fitting is applied to the Mn K-edge XANES profile of the LMR-NMC electrode after 20 cycles with the 2LPDMC. The fitting references include the pristine LMR-NMC electrode and the charged and discharged LMR-NMC electrodes from the first cycle. The spectra of the references are multiplied by their respective molar weights. The fitted profile doesn't align well with these references, indicating that substantial local atomic disordering occurred during cycling.

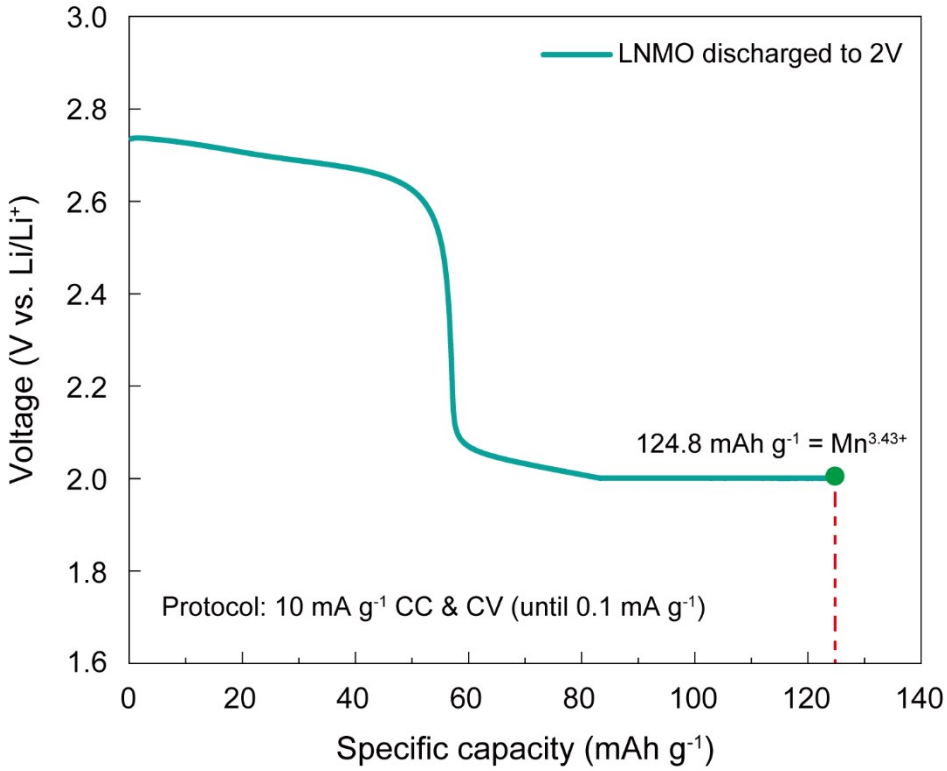

Fig. S20 Voltage profile of the spinel $LiNi_{0.5}Mn_{1.5}O_4$ (LNMO) discharged to 2.0 V (vs. Li) using a constant current-constant voltage (CC-CV) protocol. Upon reaching a potential of 2.0 V with a current density of 10 mA g^{-1}, the cell was held at a constant voltage of 2.0 V until the current density dropped to 0.1 mA g^{-1}. LNMO exhibited a capacity of 124.8 mAh g^{-1}, corresponding to a $Mn^{3.43+}$. This discharged LNMO electrode served as a reference for fitting the Mn K-edge XANES spectra of LMR-NMC reflecting cation disordering after cycling.

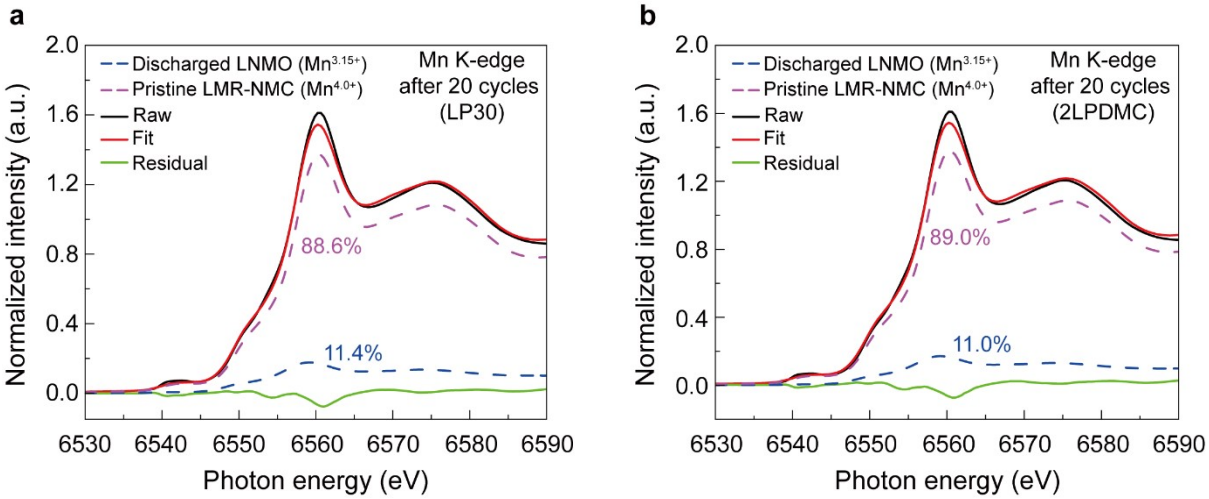

Fig. S21 Linear fitting is applied to the Mn K-edge XANES profiles of the LMR-NMC electrodes after 20 cycles with the **(a)** LP30 and **(b)** 2LPDMC. The fitting references include the pristine LMR-NMC electrode and the LNMO electrode discharged to 2.0 V. The spectra of references are multiplied by their respective molar weights. The fitted profiles exhibit a good match with these references. The fitted results indicate negligible contrast in the extent of Mn reduction after the initial 20 cycles between the two electrolytes.

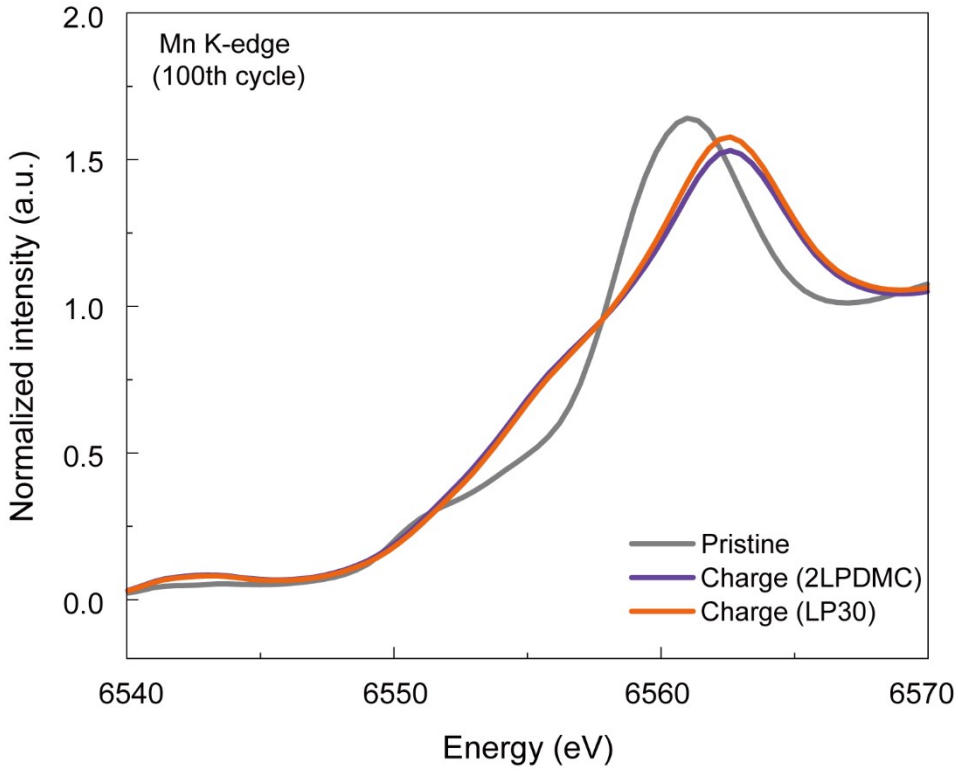

Fig. S22 Mn K-edge XANES spectra of the pristine and the charged LMR-NMC electrodes after 100 cycles with the LP30 and 2LPDMC. The oxidation states of Mn in the charged electrodes are quite similar.

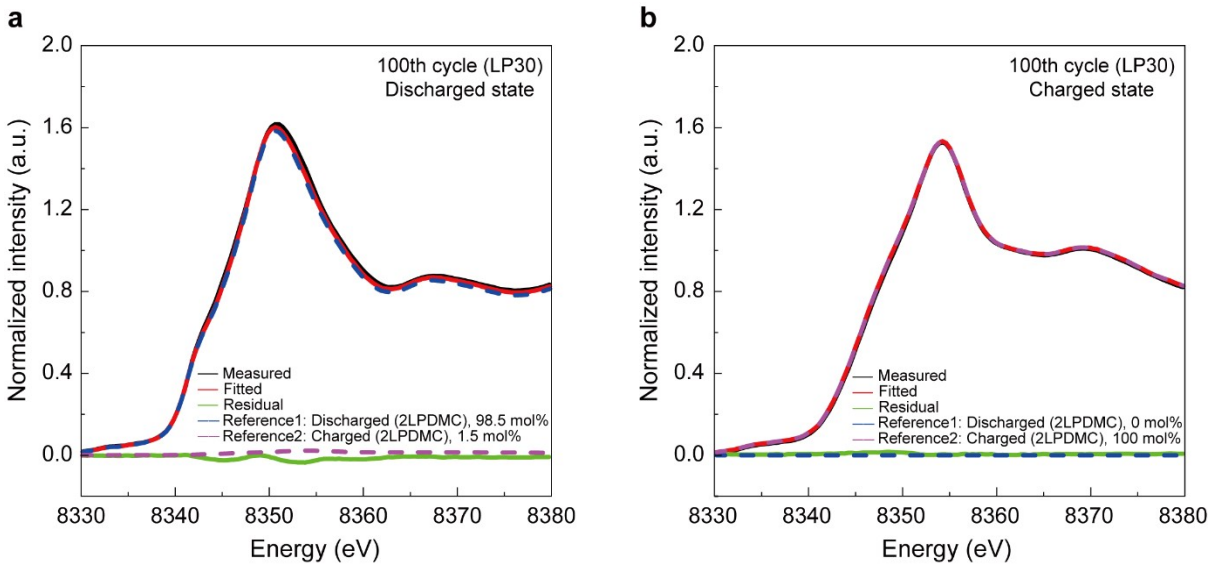

Fig. S23 Ni K-edge XANES spectra for both **(a)** discharged and **(b)** charged states of LMR-NMC electrodes after cycling for 100 cycles at 0.2C with the LP30 electrolyte. A linear fitting was conducted using the charged and discharged LMR-NMC profiles, which were obtained after 100 cycles with the 2LPDMC, as references. The results indicated that all spectra were quite similar to those obtained using the 2LPDMC. However, the discharged state with LP30 showed about 1.5 mol% less reduction.

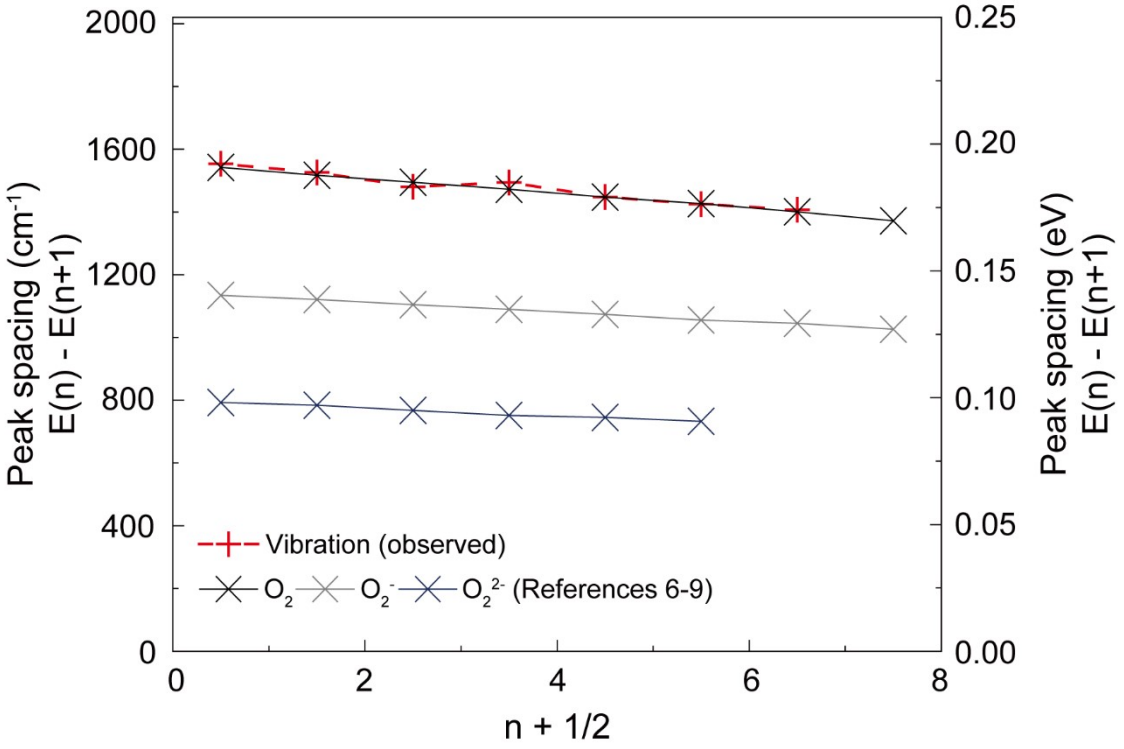

Fig. S24 The peak spacing of the vibrational progression decreases linearly with increasing energy loss, as shown in the Birge–Sponer plot, consistent with the oscillating O_2 diatomic. The initial peak spacing, equivalent to the fundamental vibration frequency, is 0.194 eV (1550 cm^{-1}) in the charged LMR-NMC, which closely corresponds to the molecular O_2 vibration[18-21]. Reference spectra for superoxide (O_2^-)[20, 21] and peroxide (O_2^{2-})[19, 21] don't match with the oscillation in the charged LMR-NMC.

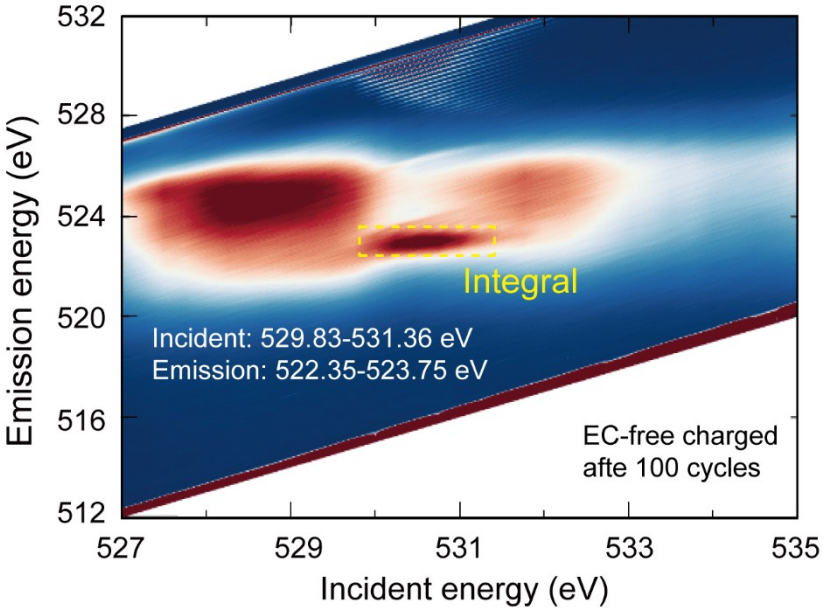

Fig. S25 RIXS O-K edge 2D-map plotted with the incident energy on the x-axis and emission energy on the y-axis. To derive relative quantitative values for oxidized anion hole feature, the area between 529.83-531.36 eV for incident energy and 522.35-523.75 eV for emission energy was integrated.

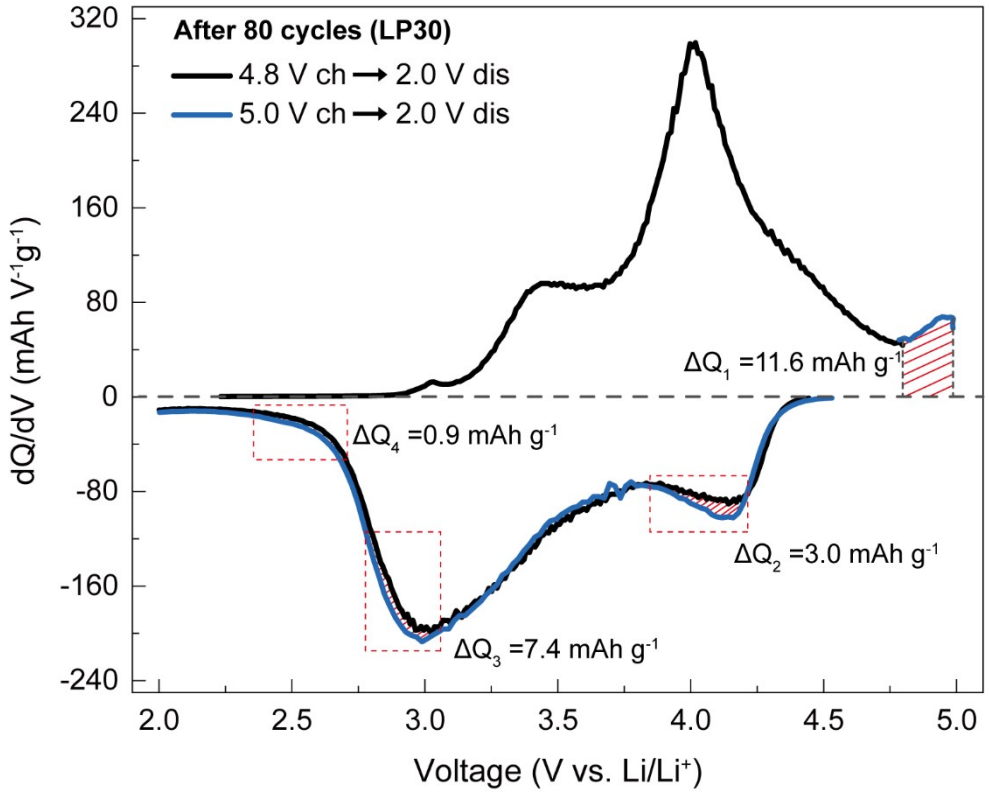

Fig. S26 The dQ/dV profiles of LMR-NMC||Li cells (CAM: 3-3.5 mg cm^{-2}, t_{Li}: 450 µm) at upper cutoff voltage of 4.8 V and 5 V after 80 cycles with LP30. During charging between 4.8 V and 5 V, an additional capacity of 11.6 mAh g^{-1} (ΔQ_1) was observed, which had not appeared up to 4.8 V due to overpotential. This additional capacity emerged reversibly across various voltage regions during discharge (ΔQ_2, ΔQ_3, and ΔQ_4), indicating that the extra capacity was due to anion oxidation.

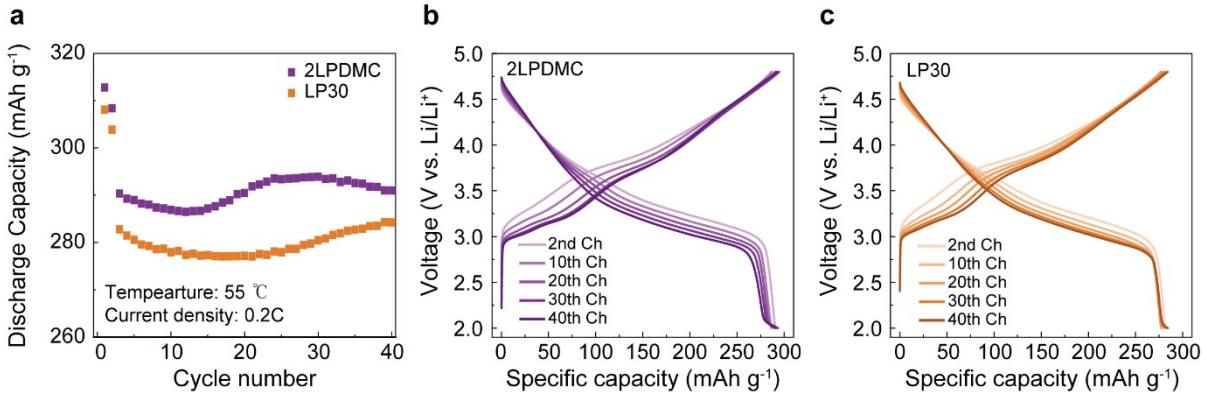

Fig. S27 (a) Cycling performance of LMR-NMC||Li cells (CAM: 3-3.5 mg cm^{-2}, t_{Li}: 450 µm) at a higher temperature of 55 °C in the 2LPDMC and LP30 electrolytes. Voltage profiles for the 5th, 10th, 20th, 40th, and 50th cycles using **(b)** 2LPDMC and **(c)** LP30. A significant reversible capacity of over 280 mAh g^{-1} could be utilized at 0.2C with both 2LPDMC and LP30. Despite the considerably high initial reversible capacity, a capacity increase due to layered-to-spinel phase transition was observed, suggesting the deeper delithiation and lithiation reactions at the higher temperature seem to have promoted spinel phase formation, even with LP30, leading to an improved cycle life.

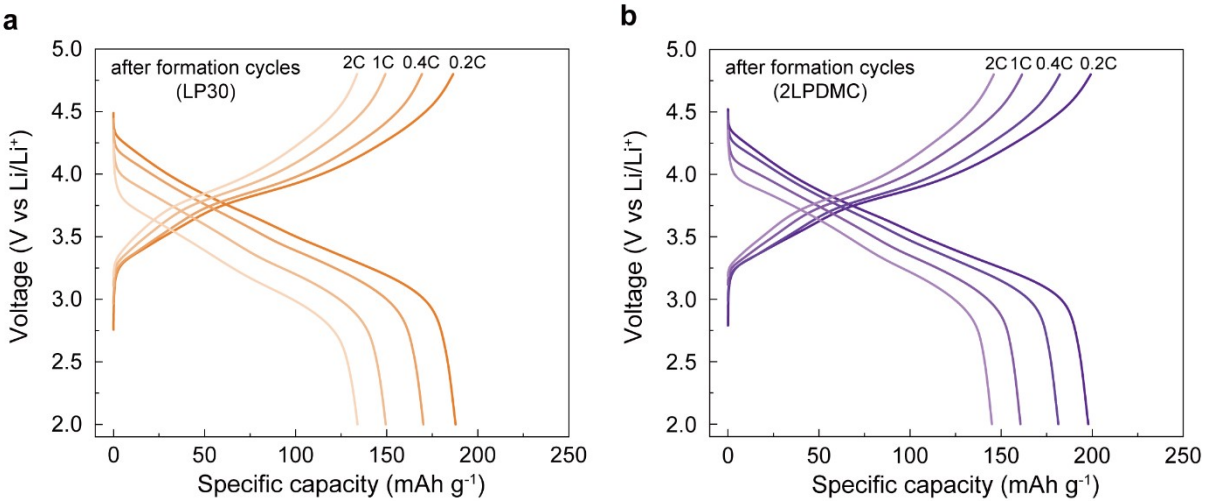

Fig. S28 Voltage profiles of LMR-NMC||Li cells (CAM: 3-3.5 mg cm^{-2}, t_{Li}: 450 µm) at various C-rates after formation cycles, using **(a), (b)** LP30 and **(c), (d)** 2LPDMC electrolytes, respectively.

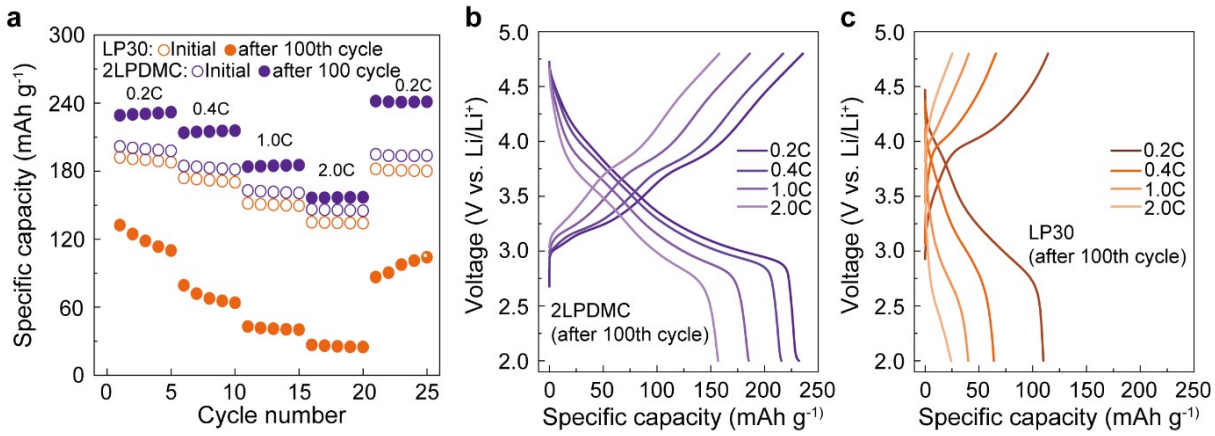

Fig. S29 (a) Rate capability of LMR-NMC||Li cells (CAM: 3-3.5 mg cm^{-2}, t_{Li}: 450 µm) with two electrolytes after formation cycles and 100 cycles, respectively. Voltage profiles of the cycled LMR-NMC at various C-rates with the **(b)** 2LPDMC and **(c)** LP30 electrolytes. Notably, in the 2LPDMC electrolyte, the practical capacity was higher after long-term cycling than the initial state at the C-rates from 0.2C to 2C, which resulted in the 11.6, 13.2, 9.4, and 2.7% improved energy densities at each C-rate. However, after cycling in the conventional electrolyte, the cathode exhibited poor rate capability, caused by the large overpotential. The results suggest that stabilizing the spinel phase and avoiding the rocksalt formation at the electrochemical interface is an effective strategy for the practical application of LMR-NMC cathodes with better lifespan and reasonable energy density retention.

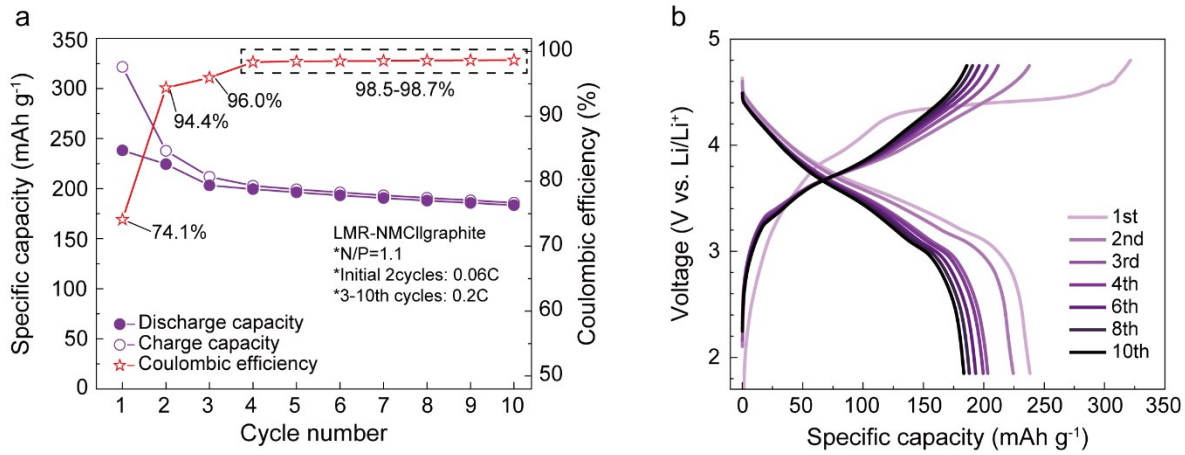

Fig. S30 (a) Cycling performance of LMR-NMC|2LPDMC|graphite full cells (N/P ratio: 1.1) and (b) the corresponding voltage profiles. The voltage ranges of the first and successive cycles were 1.85-4.8 V and 1.85-4.75 V, respectively. The C-rates are described in the figure. Due to the low CE of graphite, the full cell shows worse capacity retention than the half cells with excessive Li source.

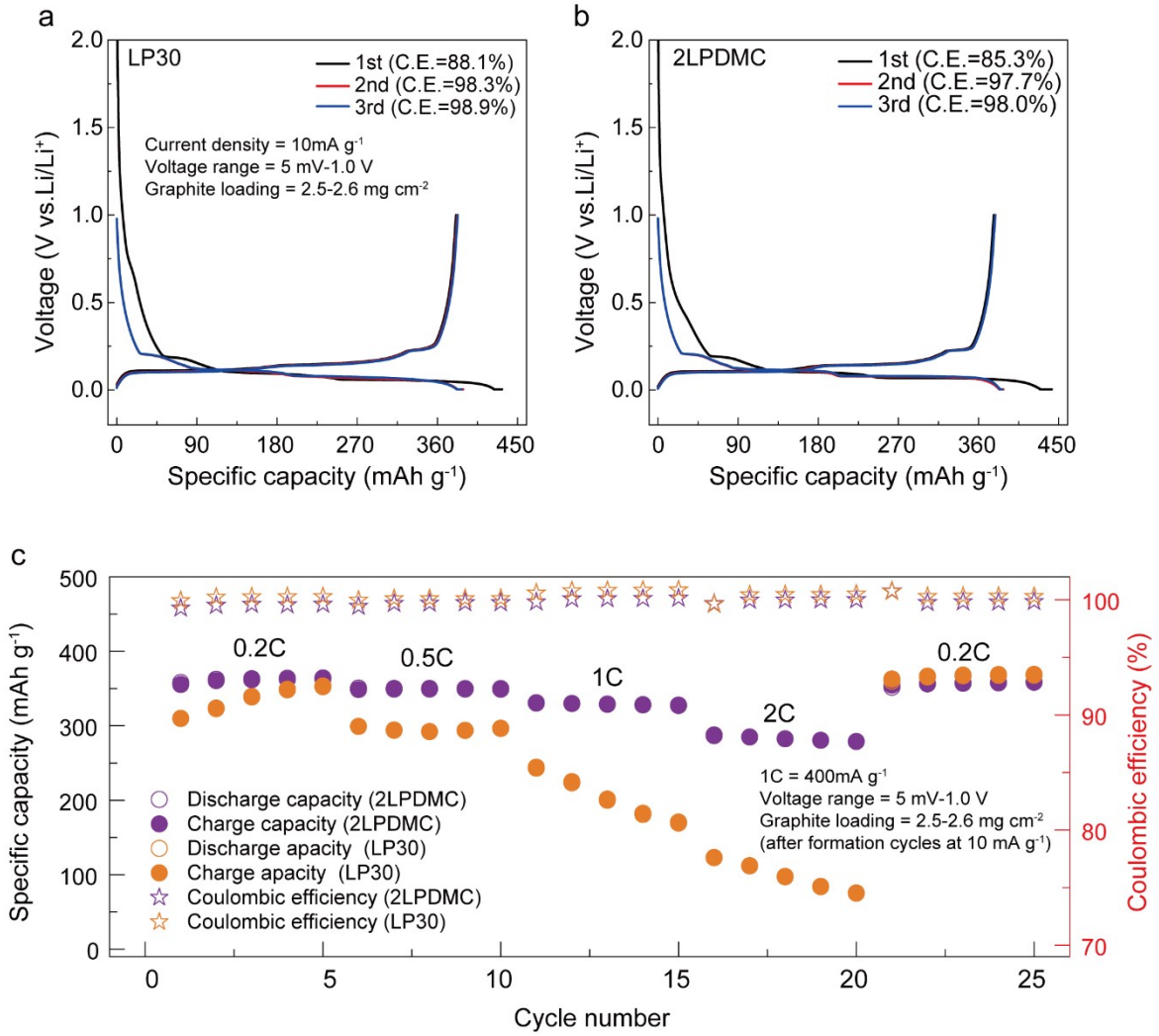

Fig. S31 Voltage profiles of the 1st, 2nd, and 3rd cycles of graphite half cells assembled with (a) LP30 and (b) 2LPDMC. The 2LPDMC cells show slightly lower CE and overpotential compared to the LP30 cells. (c) The comparison of rate performance of graphite half cells using the two electrolytes. Despite the enhanced reaction kinetics, in 2LPDMC, the CE remains relatively low across all C-rates.

Table S1. Classification of degradation cases after cycling of Lithium- and manganese-rich layered oxides in previous reports. The Case 2 accounts for the most dominant proportion.

Case [ref]	Composition	Electrolyte	Current density	Temperature	Potential range
1 [22] (ref.26 in manuscript)	$Li_{1.2}Ni_{0.2}Mn_{0.6}O_2$	1M $LiPF_6$ in EC/DMC (1:1 vol%)	0.02C	Room temp	2-4.8 V
1 [6, 23] (ref.25 in manuscript)	$Li_{1.2}Ni_{0.2}Mn_{0.6}O_2$ $Li_{1.2}Co_{0.4}Mn_{0.4}O_2$	1M $LiPF_6$ in EC/DMC (1:1 vol%)	0.08C	Room temp	2-4.8 V
1 [24] (ref.27 in manuscript)	$Li_{1.2}Ni_{0.2}Mn_{0.6}O_2$	1M $LiPF_6$ in EC/DMC (1:2 vol%)	0.1C	Room temp	2-4.7 V
1 [25] (ref.17 in manuscript)	$Li_{1.2}Ni_{0.2}Mn_{0.6}O_2$ $Li_{1.2}Ni_{0.1}Mn_{0.525}Co_{0.175}O_2$	1M $LiPF_6$ in EC/DMC (1:2 vol%)	0.33C	Room temp	2-4.6 V
1 [26] (ref.28 in manuscript)	$Li_{1.25}Ni_{0.075}Mn_{0.6}Co_{0.075}O_2$	1M $LiPF_6$ in EC/DEC (1:1 vol%)	0.07C	50°C	2-4.6 V
1 [27] (ref.31 in manuscript)	$Li_{1.2}Ni_{0.13}Mn_{0.54}Co_{0.13}O_2$	1 M LiPF6 in EC/DMC (1:2 vol%)	0.1C	Room temp	2-4.6 V
1[28] (ref.9 in manuscript)	$Li_{1.2}Ni_{0.2}Mn_{0.6}O_2$	1M $LiPF_6$ in EC/DMC (1:1 vol%)	0.1C	Room temp	2-4.8 V
2 [29] (ref.29 in manuscript)	$Li_{1.2}Ni_{0.2}Mn_{0.6}O_2$	1M $LiPF_6$ in EC/DEC (1:1 vol%)	0.2C	Room temp	2-4.8 V
2 [30] (ref.30 in manuscript)	$Li_{1.2}Mn_{0.61}Ni_{0.18}Mg_{0.01}O_2$	no mention	0.1C	Room temp	2-4.5V
3 [31] (ref.19 in manuscript)	$Li_{1.18}Ni_{0.21}Mn_{0.53}Co_{0.08}O_2$	1.3 M $LiPF_6$ in FEC/DMC/HFE (3:8:9 vol%) +additives	1C(ch) /2C(dis)	Room temp	2-4.55 V

* Case1: coexistence of spinel and rocksalt nano-domains on the surface.

* Case2: layered-to-rocksalt surface reconstruction with the preserved layered structure.

* Case3: oxygen vacancy formation & diffusion without phase transition.

* Abbreviation description: EC=ethylene carbonate, DMC=dimethyl carbonate, DEC=diethyl-carbonate, HFE=hydrofluoroether

Table S2. Structural parameters obtained from the Rietveld refinement of XRD patterns of the synthesized LMR-NMC powder with the space group of *C*2/*m*. Since it is difficult to distinguish Ni, Co, and Mn using X-ray, all transition metals are labeled as Mn.

a = 4.9466 (10) Å, b = 8.5664 (19) Å, c = 5.0368 (9) Å, ß = 109.2557 (127) °

Site	Occupancy	x	y	Z
2*c*	98.2% Li, 1.8% Ni	0	0	0.5
4*h*	98.2% Li, 1.8% Ni	0	0.66667	0.5
2*b*	19% Li, 81% TM	0.500	0.5	0
4*g*	20% Li, 80% Ni	0.160	0.144 (1)	0
4*i*	100% O	0.500	0	0.217 (7)
8*j*	100% O	0.1600	0.329 (2)	0.232 (3)

Table S3. Detailed information on the configuration and operating protocols of coin-cells.

Cell configuration (Corresponding figures)	Active material loading (mg cm^{-2})	A:B:C weight ratio	Thickness of anode (μm)	Amount of electrolyte (μl)	**[Formation]** Voltage range C-rate Temperature	**[Cycling]** Voltage range C-rate Temperature
LMR-NMC|1M LP30|Li LMR-NMC|2LPDMC|Li **(All except the conditions below)**	3.0-3.5	80:10:10	450	100	2-4.8 V 0.06C 30℃	2-4.8 V 0.2C 30℃
LMR-NMC|1M LP30|Li LMR-NMC|2LPDMC|Li **(Fig. S6)**	8.0	90:5:5	450	100	2-4.8 V 0.06C 30℃	2-4.8 V 0.2C 30℃
LMR-NMC|1M LP30|Li LMR-NMC|2LPDMC|Li **(Fig. S27)**	3.0-3.5	80:10:10	450	100	2-4.8 V 0.06C 55℃	2-4.8 V 0.2C 55℃
LMR-NMC|1.5M LP30|Li LMR-NMC|1LPDMC|Li LMR-NMC|1.5LPDMC|Li **(Fig. S3)**	3.0-3.5	80:10:10	450	100	2-4.8 V 0.06C 30℃	2-4.8 V 0.2C 30℃
graphite|LP30|Li graphite|2LPDMC|Li **(Fig. S30)**	2.5-2.6	94:4.6:1.4	450	100	5 mV-1.0 V 10 mA g^{-1} 30℃	5 mV-1.0 V 10 mA g^{-1} 30℃
LMR-NMC|2LPDMC|graphite **(Fig. S31)**	3.0-3.5 (cathode)	80:10:10/ 94:4.6:1.4 (anode)	45 (N/P=1.1)	100	1.85-4.8 V 0.06C 30℃	1.85-4.75 V 0.2C 30℃

* Active material loading: mass of active material loaded on the electrode
* A:B:C mass ratio: weight ratio of 'active material : binder : conductive agent'
* To compensate for the relatively thinner graphite electrode compared to Li metal, a spacer that is 300 μm thicker than that used in a half-cell was utilized

Table S4. Comparison of electrochemical cycling conditions and cycle life with those in state-of-the-art research on Li-rich and Mn-rich layered oxides.

No.	Materials	Electrolytes	Mass loading (mg cm^{-2})	Current rate	Voltage range (V vs. Li/Li^+)	Capacity retention per 50 cycles
1[32]	$Li_{1.25}Ni_{0.125}Mn_{0.625}O_2$ $Li_{1.25}Co_{0.25}Mn_{0.5}O_2$	1 M $LiPF_6$ in EC/DMC	Not applicable	0.1C	2-4.6	Not applicable
2[5]	$Li_{1.16}Ni_{0.28}Mn_{0.56}O_2$	1 M $LiPF_6$ in EC/DMC (1:1 vol%)	10	C/3	2.0-4.5	~87%
3[6]	$Li_{1.2}Ni_{0.2}Mn_{0.6}O_2$	1 M $LiPF_6$ in EC/DMC (1:1 vol%)	4-6	0.1C	2-4.8	~88%
4[7]	$Li_{1.2}Ni_{0.13}Mn_{0.54}Co_{0.13}O_2$	1 M $LiPF_6$ in EC/DMC (1:1 vol%)	10	0.4C	2-.8	~85%
Our work	$Li_{1.17}Ni_{0.21}Mn_{0.55}Co_{0.07}O_2$	1 M $LiPF_6$ in EC/DMC (1:1vol%)	8	0.2	2-4.8	62.8%
Our work	$Li_{1.17}Ni_{0.21}Mn_{0.55}Co_{0.07}O_2$	2M $LiPF_6$ in DMC (2LPDMC)	8	0.2	2-4.8	93.0%

1. Eum et al., *Energy Environ. Sci.* **2023**, 16, 673-686

2. Choi et al., *Energy Environ. Sci.* **2024**, 17, 4634-4645

3. Li et al., *Nat. Mater.* **2023**, 22, 1370-1379

4. Marie et al., *Nat. Mater.* **2024**, 23, 818-825

Table S5. Changes of R_{ct} according to the electrolytes. The LMR-NMC cycled with LP30 showed a significant increase of $R_{ct.}$

	LP30 (formation)	LP30 (50cy)	LP30 (100cy)	2LPDMC (formation)	2LPDMC (50cy)	2LPDMC (100cy)
R_{ct} (Ω)	46.59	1293	2587	48.2	81.32	71.17

Table S6. ICP-AES results of dissolved transition metals (TM) after long-term cycling show that poor interfacial stability of LMR-NMC with LP30 triggered TM dissolution.

Sample	Ni (ppb)	Mn (ppb)	Co (ppb)
2LPDMC	20	20	-
LP30	140	300	70

Table S7. The results of linear fitting of the Mn K-edge XANES profile about LMR-NMC electrode after 20 and 100 cycles with the LP30 and 2LPDMC. The fitting references were the pristine LMR-NMC electrode and the 2 V-discharged LNMO electrode.

	LP30 (20cy)	LP30 (100cy)	2LPDMC (20cy)	2LPDMC (100cy)
Ratio of LMR-NMC (Mn^{4+})	88.6%	81.8%	89.0%	67.6%
Ratio of discharged LNMO ($Mn^{3.43+}$)	11.4%	18.2%	11.0%	32.4%
Oxidation state	3.94	3.90	3.94	3.82
Capacity of Mn redox (mAh $g^{-1}_{LMR-NMC}$)	11.9	19.9	11.9	35.8

Table S8. The amount of reversible capacity of each redox of the LMR-NMC after 100 cycles. The reversible capacity of each redox reaction after cycling can be specified by using the absolute quantitative values of cation redox, as obtained through XANES analyses, and the relative values of anion redox, as determined through the RIXS analyses. We already know the total reversible capacity of all redox reactions from the electrochemical cycling test (**Fig. 1(a)**), as well as the specific contribution of Mn redox (as mentioned in **Table S3**). Therefore, the remaining capacity should correspond to Ni and Co cation redox or oxygen anion redox. Given that the oxidation state of Ni cation redox is almost same (**Supplementary Fig. 19)** and considering the relative 66.9 % lower utilization of anion redox with the LP30 electrolyte after 100 cycles (**Fig. 4(g)**), we can distinguish between the absolute quantitative values of (Ni+Co) redox and anion redox.

	Pristine (initial state)	LP30 (100cy)	2LPDMC (100cy)	Relative Ratio (100cy) (LP30/2LPDMC)
Capacity of Mn redox (mAh $g^{-1}_{LMR-NMC}$)	0	19.9	35.8	0.556
Capacity of O redox (mAh $g^{-1}_{LMR-NMC}$)	94.3	50.4	75.3	0.669
Capacity of Ni+Co redox (mAh $g^{-1}_{LMR-NMC}$)	109.3	106.4	108.0	0.985
Total capacity (mAh $g^{-1}_{LMR-NMC}$)	203.6	176.7	219.1	0.806

References

1. M. M. Thackeray, S.-H. Kang, C. S. Johnson, J. T. Vaughey, R. Benedek and S. Hackney, *Journal of Materials chemistry*, 2007, **17**, 3112-3125.
2. M. Armand and J.-M. Tarascon, *nature*, 2008, **451**, 652-657.
3. B. Obama, *Science*, 2017, **355**, 126-129.
4. W. E. Gent, K. Lim, Y. Liang, Q. Li, T. Barnes, S.-J. Ahn, K. H. Stone, M. McIntire, J. Hong and J. H. Song, *Nature communications*, 2017, **8**, 2091.
5. G. Choi, U. Chang, J. Lee, K. Park, H. Kwon, H. Lee, Y.-I. Kim, J. H. Seo, Y.-C. Park and I. Park, *Energy & Environmental Science*, 2024, **17**, 4634-4645.
6. B. Li, Z. Zhuo, L. Zhang, A. Iadecola, X. Gao, J. Guo, W. Yang, A. V. Morozov, A. M. Abakumov and J.-M. Tarascon, *Nature Materials*, 2023, **22**, 1370-1379.
7. J.-J. Marie, R. A. House, G. J. Rees, A. W. Robertson, M. Jenkins, J. Chen, S. Agrestini, M. Garcia-Fernandez, K.-J. Zhou and P. G. Bruce, *Nature Materials*, 2024, 1-8.
8. K.-W. Nam, M. G. Kim and K.-B. Kim, *The Journal of Physical Chemistry C*, 2007, **111**, 749-758.
9. W. M. Dose, I. Temprano, J. P. Allen, E. Björklund, C. A. O'Keefe, W. Li, B. L. Mehdi, R. S. Weatherup, M. F. De Volder and C. P. Grey, *ACS Applied Materials & Interfaces*, 2022, **14**, 13206-13222.
10. B. L. Rinkel, J. P. Vivek, N. Garcia-Araez and C. P. Grey, *Energy & environmental science*, 2022, **15**, 3416-3438.
11. J. E. Puskas, K. S. Seo and M. Y. Sen, *European Polymer Journal*, 2011, **47**, 524-534.
12. B. L. Rinkel, D. S. Hall, I. Temprano and C. P. Grey, *Journal of the American Chemical Society*, 2020, **142**, 15058-15074.
13. R. Jung, M. Metzger, F. Maglia, C. Stinner and H. A. Gasteiger, *The journal of physical chemistry letters*, 2017, **8**, 4820-4825.
14. G. Lim, D. Shin, K. H. Chae, M. K. Cho, C. Kim, S. S. Sohn, M. Lee and J. Hong, *Advanced Energy Materials*, 2022, **12**, 2202049.
15. W. M. Dose, W. Li, I. Temprano, C. A. O'Keefe, B. L. Mehdi, M. F. De Volder and C. P. Grey, *ACS Energy Letters*, 2022, **7**, 3524-3530.
16. A. T. Freiberg, M. K. Roos, J. Wandt, R. de Vivie-Riedle and H. A. Gasteiger, *The Journal of Physical Chemistry A*, 2018, **122**, 8828-8839.
17. R. Jung, M. Metzger, F. Maglia, C. Stinner and H. A. Gasteiger, *Journal of The Electrochemical Society*, 2017, **164**, A1361.
18. C. Århammar, A. Pietzsch, N. Bock, E. Holmström, C. M. Araujo, J. Gråsjö, S. Zhao, S. Green, T. Peery and F. Hennies, *Proceedings of the National Academy of Sciences*, 2011, **108**, 6355-6360.
19. R. A. House, G. J. Rees, M. A. Pérez-Osorio, J.-J. Marie, E. Boivin, A. W. Robertson, A. Nag, M. Garcia-Fernandez, K.-J. Zhou and P. G. Bruce, *Nature Energy*, 2020, **5**, 777-785.
20. R. Sharpe, R. A. House, M. J. Clarke, D. Förstermann, J.-J. Marie, G. Cibin, K.-J. Zhou, H. Y. Playford, P. G. Bruce and M. S. Islam, *Journal of the American Chemical Society*, 2020, **142**,

21799-21809.
21. P. M. Radjenovic and L. J. Hardwick, *Physical Chemistry Chemical Physics*, 2019, **21**, 1552-1563.
22. B. Xu, C. R. Fell, M. Chi and Y. S. Meng, *Energy & Environmental Science*, 2011, **4**, 2223-2233.
23. B. Li, Z. Zhuo, L. Zhang, A. Iadecola, X. Gao, J. Guo, W. Yang, A. V. Morozov, A. M. Abakumov and J.-M. Tarascon, *Nature Materials*, 2023, 1-10.
24. J. Zheng, M. Gu, J. Xiao, P. Zuo, C. Wang and J.-G. Zhang, *Nano letters*, 2013, **13**, 3824-3830.
25. M. Gu, I. Belharouak, J. Zheng, H. Wu, J. Xiao, A. Genc, K. Amine, S. Thevuthasan, D. R. Baer and J.-G. Zhang, *ACS nano*, 2013, **7**, 760-767.
26. C. S. Johnson, N. Li, C. Lefief, J. T. Vaughey and M. M. Thackeray, *Chemistry of Materials*, 2008, **20**, 6095-6106.
27. H. Liu, K. J. Harris, M. Jiang, Y. Wu, G. R. Goward and G. A. Botton, *ACS nano*, 2018, **12**, 2708-2718.
28. W. Hua, S. Wang, M. Knapp, S. J. Leake, A. Senyshyn, C. Richter, M. Yavuz, J. R. Binder, C. P. Grey and H. Ehrenberg, *Nature communications*, 2019, **10**, 5365.
29. B. Wen, F. N. Sayed, W. M. Dose, J. K. Morzy, Y. Son, S. Nagendran, C. Ducati, C. P. Grey and M. F. De Volder, *Journal of Materials Chemistry A*, 2022, **10**, 21941-21954.
30. A. Boulineau, L. Simonin, J.-F. Colin, C. Bourbon and S. Patoux, *Nano letters*, 2013, **13**, 3857-3863.
31. P. M. Csernica, S. S. Kalirai, W. E. Gent, K. Lim, Y.-S. Yu, Y. Liu, S.-J. Ahn, E. Kaeli, X. Xu and K. H. Stone, *Nature Energy*, 2021, **6**, 642-652.
32. D. Eum, H.-Y. Jang, B. Kim, J. Chung, D. Kim, S.-P. Cho, S. H. Song, S. Kang, S. Yu and S.-O. Park, *Energy & Environmental Science*, 2023, **16**, 673-686.